# CO$_2$ and CO temporal variability over Mexico City from ground-based total column and surface measurements

Noémie Taquet[1], Wolfgang Stremme[1], María Eugenia González del Castillo[1], Victor Almanza[1], Alejandro Bezanilla[1], Olivier Laurent[2], Carlos Alberti[3], Frank Hase[3], Michel Ramonet[2], Thomas Lauvaux[4], Ke Che[4], Michel Grutter[1]

[1]Instituto de Ciencias de la Atmósfera y Cambio Climático, Universidad Nacional Autónoma de México, México
[2]Laboratoire des Sciences du Climat et de l'Environnement (LSCE), IPSL, CEA-CNRS-UVSQ, Université Paris-Saclay, Gif-sur-Yvette, France
[3]Institute of Meteorology and Climate Research (IMK-ASF), Karlsruhe Institute of Technology (KIT), Karlsruhe, Germany
[4]Groupe de Spectrométrie Moléculaire et Atmosphérique (GSMA), Université de Reims-Champagne Ardenne, UMR CNRS 7331, Reims, France

*Correspondence to*: Noémie Taquet (noemi.taquet@gmail.com)

**Abstract**.

Accurate estimates of greenhouse gas emissions and sinks are critical for understanding the carbon cycle and identifying key drivers of anthropogenic climate change. In this study, we investigate the variability of CO and CO$_2$ concentrations and their ratio over the Mexico City Metropolitan Area (MCMA) from long-term time-resolved columnar measurements at three stations, using solar absorption Fourier transform infrared spectroscopy (FTIR). Using a simple model and the mixed layer height derived from a ceilometer, we determined the CO and CO$_2$ concentration in the mixed layer from the total column measurements and found good agreement with surface cavity ring-down spectroscopy measurements. In addition, we used the diurnal pattern of CO columnar measurements at specific time intervals to estimate an average growth rate that, when combined with the space-based TROPOMI CO measurements, allowed deriving annual CO and CO$_2$ MCMA emissions from 2016 to 2021. A decrease of more than 50% of the CO emissions was found during the COVID19 lockdown period with respect to the year 2018. These results demonstrate the feasibility of using long-term EM27/Sun column measurements to monitor the annual variability of anthropogenic CO$_2$ and CO emissions in Mexico City without recourse to complex transport models. This simple methodology could be adapted to other urban areas if the orography favours low ventilation for several hours per day, which allows that column growth rate to be dominated by emission flux.

## 1 Introduction

The greenhouse gas (GHG) mitigation strategies implemented in megacities following the 1997 Kyoto Protocol and the 2015 Paris Agreement play a crucial role in the global action plan to mitigate climate change, given that cities are accountable for more than 70% of the global anthropogenic emissions (Duren and Miller, 2012). With the recent progress in space-based and ground-based remote GHG measurements in terms of accuracy, spatial coverage, resolution and temporal frequency, GHG emissions can increasingly be constrained by comparing bottom-up and top-down estimates. Top-down approaches are generally based on ground- or space-based atmospheric measurements coupled with inverse modelling, using 3D-Eulerian (i.e: WRF-Chem) or Lagrangian and hybrid (i.e: X-STILT, Hysplit) approaches (Wu et al., 2018, Che et al., 2022; Lian et al., 2023). The quantification of anthropogenic CO$_2$ enhancements from cities using satellite data e.g: GOSAT (Wang et al.,

45  2019), OCO-2 (Ye et al., 2020) or TanSat (Liu et al., 2018) is still challenging due to the sparsity of the

46  observations, the low signal from the anthropogenic contribution compared to the background levels and biogenic

47  contribution, and some inconveniences inherent to space-measurements such as the non-negligible aerosol effects

48  (Wang et al., 2020 and references therein). Some studies have estimated the urban enhancements of anthropogenic

49  $CO_2$ concentrations along with CO and $NO_2$ from satellite measurements, as these air pollutants can serve as tracers

50  of anthropogenic $CO_2$ (Silva et al.,2013; Park et al., 2021 and references therein). The $CO/CO_2$ ratio is often used

51  to determine the combustion efficiency of the cities (Park et al., 2021 and references therein). With the

52  development of a new generation of space-based observatories, such as Sentinel-5P and OCO-2,3, the evolution

53  of GHGs at the city scale can now be characterised with a finer temporal and spatial resolution (Kiel et al., 2021)

54  but more validation efforts are needed. As inverse modelling is likely undermined by the approximations used for

55  defining the emission patterns, transport processes and meteorology, top-down approaches may lead to

56  discrepancies in emissions estimates, in particular in sites with complex orography.

57  Ground-based total column FTIR instruments provide valuable long-time concentration measurements of

58  GHG and pollutant reactive species, as well as anthropogenic tracers, constituting a key element to validate

59  regional and local inventories. Some studies reported estimates of $CO_2$ and $CH_4$ emissions from large urban areas

60  (Babenhauserheide et al., 2018 in Tokyo; Hedelius et al., 2018 in the California Southern Coast Air Basin

61  California megacity), using data from high-resolution FTIR instruments (i.e: Bruker IFS120/5HR) contributing to

62  the Total Column Carbon Observing Network (TCCON). Nevertheless, only a few TCCON stations are located in

63  urban areas (Toon et al., 2009; Chevallier et al., 2011; Sussman et al., 2020). The development of the COllaborative

64  Carbon Column Observing Network (COCCON, Frey et al., 2019), using a new generation of portable low spectral

65  resolution FTIR spectrometers (EM27/SUN, Gisi et al., 2012; Hase et al., 2016) able to simultaneously measure

66  the $CO_2$, CO, $H_2O$ and $CH_4$ average total columns with a similar quality as TCCON, has considerably densified

67  the number of measurements in urban environments. Some studies reported emission estimates for big cities by

68  means of the deployment of several EM27/SUN instruments at strategic sites throughout the cities (Hase et al.,

69  2015 and Zhao et. al., 2019 in Berlin; Vogel et al., 2019 in Paris; Makarova et al., 2021 in St Petersbourg; Zhou et

70  al., 2022 in Beijing and Xianghe; Che et al. 2022, in Beijing; Rißmann et al., 2022 for Munich) coupling columnar

71  measurements with inverse modelling. Most of these studies were based on short-term campaign observations,

72  applying the Differential Column Methodology (DCM, Chen et al., 2016) or dedicated dispersion models (Hase

73  et al., 2016), coupled with simple mass balance-based methods or inverse modelling to derive emissions. Most of

74  these studies reported significant discrepancies between the estimates, depending on the models used (Viatte et

75  al., 2017).

76  In this study, we aimed to determine the Mexico City Metropolitan Area (MCMA) $CO_2$ and CO emissions

77  using ground-based FTIR and surface measurements, without resorting to complex dispersion and/or chemistry

78  transport models. The MCMA, with a population around 22 million inhabitants, is in the top ten most populous

79  cities in the world and ranks among the major emitters of GHGs in North America. The available information of

80  GHGs emission estimates are mainly based on the inventories reported by the Ministry of the Environment of

81  Mexico City (SEDEMA), which is updated every two years, but lagging several years behind. In the report based

82  on 2018, the latest published before the COVID19-lock-down (2020), a total emission of 75.2 Mt CO2-eq is

83  estimated for the MCMA, 87% of which is attributed to fossil fuel combustion and 58% originates from the

84  transport sector (SEDEMA Inventory, 2018). The Mexico City government is actively engaged in the C40 Climate

85  Change Program and implemented significant policy measures since 2008, including promoting sustainable
86  transportation systems, implementing energy efficiency measures, increasing the use of renewable energy sources,
87  and adopting green building practices. On a national scale, the country is committed to reduce its GHGs emissions
88  by 35% by 2030 with respect to its base level, as stated in the last Nationally Determined Contributions report
89  (NDC-2022, UNFCCC). To assess the effect of the national and local mitigation policies, the installation of
90  ground-based GHG measurement networks and the refinement of bottom-up estimates by comparing them with
91  the top-down method (i.e: inverse modelling) is of critical importance to obtain a comprehensive GHGs database
92  that can serve as follow-up of the mitigation actions.

93  The Institute of Atmospheric Sciences and Climate Change (ICAyCC, Spanish acronym) at UNAM
94  (Universidad Nacional Autónoma de México) deployed in the last decade a wide range of surface gas sensors and
95  ground-based remote sensing instruments across the MCMA (Grutter, et al., 2003; Molina et al., 2010; Bezanilla
96  et al., 2014; Stremme et al., 2009; 2013; Baylon et al., 2017) in the frame of research projects related to air quality
97  assessment, atmospheric monitoring and satellite products validation. Since 2013, UNAM has contributed to the
98  Network for the Detection of Atmospheric Composition Change (NDACC), performing continuous composition
99  measurements of the free troposphere from the high altitude Altzomoni Atmospheric Observatory (ALTZ) station,
100 located 60 km southeast of Mexico City at 3985 m a.s.l. Baylon et al., (2017) reported the background $CO_2$
101 variability and trend from this station between 2013 and 2016. Stremme et al., (2013) reported the first top-down
102 estimate of carbon monoxide (CO) emissions for the MCMA, based on FTIR CO total column measurements and
103 the Infrared Atmospheric Sounding Interferometer (IASI) data. These authors derived the $CO_2$ emissions for the
104 MCMA using the CO emission estimates and the average $CO/CO_2$ ratio reported in Grutter (2003), using FTIR
105 measurements. In 2018, the Mexican/French "Mexico City's Regional Carbon Impacts (MERCI-CO2)" project
106 (coordinated by UNAM and LSCE) was launched aiming to assess the $CO_2$ emissions from MCMA using
107 EM27/SUN measurements and inverse modelling to evaluate the effectiveness of the mitigation strategies
108 implemented by the local authorities. Xu et al., (submitted) examined the performance of a modelling system based
109 on WRF-Chem to assess the whole-city emissions using the EM27/SUN measurements deployed in the frame of
110 the MERCI-CO2 project. The complex orography of the region posed a challenge in the atmospheric transport
111 simulations and thus for the top-down estimates using inverse modelling. Indeed, Mexico City is situated in a high
112 altitude basin (~2300 m. a.s.l.), surrounded by mountains reaching up to 5.6 km a.s.l., and is prone to accumulate
113 anthropogenic emissions, especially during the dry season, when the atmospheric boundary layer ventilation is
114 limited (Burgos-Cuevas et al., 2023). The boundary layer dynamics in the basin and the wind surface circulation
115 is complex, due to the temperature contrasts and rough topography.

116 In this study, we report the long-term (2013-2021) variability of the $CO_2$ and CO total columns and
117 surface concentrations (from 2014) over the MCMA using ground-based FTIR and surface Cavity Ring-Down
118 Spectroscopic (CRDS) measurements. Using the mixed layer height data from the continuous ceilometer
119 measurements at UNAM, we examined the consistency of the surface and total column measurements of our
120 network. We also determined an average $CO/CO_2$ ratio based on FTIR and surface measurements at different
121 temporal resolutions (from daily to intraday). Then, using the spatial distribution of TROPOMI CO column
122 measurements, we explore the potential of our FTIR network to capture the variability of the megacity CO and

123     $CO_2$ emissions using a simplified model, i.e.: without recourse to complex numerical simulations. Our estimates

124     are compared with the available bottom-up and previous top-down estimates.

**2 Sites, instrumentation and measurement protocols**

126     We used in this study the column-averaged dry-air mole fractions of $CO_2$ and CO ($XCO_2$ and XCO) from

127     three permanent FTIR stations distributed in a radius of 100 km around MCMA (Fig. 1), and the surface

128     measurements performed at UNA and ALTZ sites. The measurement periods for the different instruments at each

129     site are reported in Table 1. The VAL station is located at the northern part of the city in a highly industrialised

130     zone. The UNA station is situated at the south of the city in the main campus of UNAM. The third station is the

131     ALTZ background site (3985 m a.s.l.), located 60 km ESE from UNAM, within the Izta-Popo National Park. The

132     equipment of the different stations and measurement protocols are described in the following sub-sections.
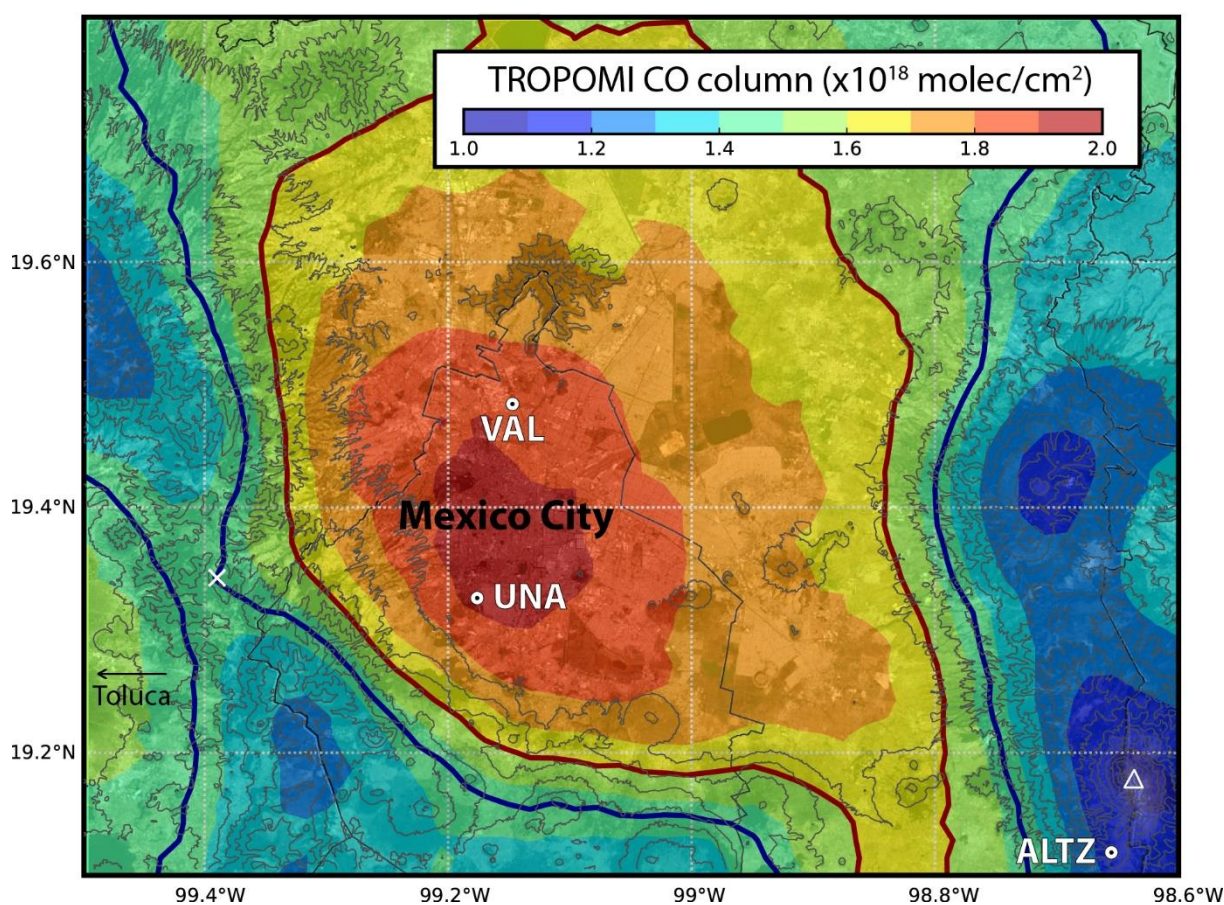
133 **Figure 1: Map of the ALTZ, UNA and VAL stations and average distribution (2018-2022) of carbon monoxide total**
134 **columns over the Mexico City Metropolitan Area (MCMA) calculated from the TROPOMI CO product. Red and blue**
135 **contour lines represent the inner and outer area used to calculate the effective area (see details in text). The cross symbol**
136 **indicates the smallest CO total column value observed upwind the city at the elevation of the Mexican basin, which is**
137 **used to estimate the background. The average total column can be decomposed into two main contributors: i) a**
138 **background of around $1.45 \times 10^{18}$ molec.cm$^{-2}$ (limits represented by blue contour lines) and ii) the local influence**
139 **corresponding to the carbon monoxide emitted on the same day. The total columns are highly influenced by the**
140 **topography which is clearly visible over the highest terrains of the region, near to the Popocatepétl and Iztaccíhuatl**
141 **volcanoes at the south east of Mexico City. The mountains of Ajusco are located southwest of Mexico City. The**
142 **enhancement in the center of the metropolitan area reflects the carbon monoxide locally emitted on the same day.**

146 *Table1: Instrumentation and measurement periods used in this study.*

| Station | Instrument | Measurement period | Product |
|---|---|---|---|
| ALTZ (19.119°N, 98.655°W 3.99 km a.s.l.) | IFS120/5HR | 01/01/2013 - 01/06/2021 | XCO and XCO$_2$ |
| | EM27/SUN #038 | 21/10/2020 - 20/12/2020 & 10/02/2021 - 22/02/2021 | XCO and XCO$_2$ |
| | EM27/SUN #104 | 07/02/2020 - 18/02/2020 | XCO and XCO$_2$ |
| | CRDS G2401 Picarro | 15/11/2015 - 01/06/2021 | Surface CO and CO$_2$ |
| UNA (19.326°N, 99.176°W 2.28 km a.s.l.) | Vertex | 15/11/2015 - 20/06/2017 | XCO |
| | EM27/SUN #038 EM27/SUN #062 | 07/05/2021 - 25/05/2021 17/03/2016 - 01/06/2017 01/06/2017 - 01/06/2021 | XCO and XCO$_2$ XCO$_2$ XCO and XCO$_2$ |
| | EM27/SUN #104 | 04/04/2019 - 19/09/2019 | XCO and XCO$_2$ |
| | CDRS G2401 Picarro | 15/11/2015 - 01/06/2021 | Surface CO and CO$_2$ |
| | CL31 Vaisala ceilometer | 15/11/2015 - 01/06/2021 | Mixed Layer Height |
| VAL (19.484°N, 99.147°W 2.26 km a.s.l.) | EM27/SUN #104 | 23/09/2019 - 01/06/2021 | XCO and XCO$_2$ |

147

**2.1 The UNA station: Total columns, surface concentrations and mixed-layer height measurements**

149     Atmospheric total columns of several gas species, such as $O_3$, $NH_3$, $CH_4$, CO, and HCHO have
150 continuously been measured at UNA since 2010 (Bezanilla et al., 2014; Plaza-medina et al., 2017; Baylon et al.,
151 2017; Rivera-Cardenas et al., 2021; Herrera et al., 2022) using solar absorption FTIR spectroscopy.
152 Measurements are performed in the mid-infrared (MIR) and near-infrared (NIR) spectral ranges using a Bruker
153 model Vertex 80 spectrometer. The instrument has a Maximum optical Path Difference (MPD) of 12 cm
154 (corresponding to a spectral resolution of 0.075 cm$^{-1}$) and is equipped with two detectors, a liquid-nitrogen cooled
155 mercury-cadmium-telluride (MCT) and InGaAs detectors. Solar absorption measurements are performed using a
156 home-built solar tracker. A full description of the instrumental set-up and measurement protocols is given in
157 Bezanilla et al. (2014) and Plaza-Medina et al. (2017). The CO measurements are routinely performed in the MIR
158 spectral range with a spectral resolution of 0.1 cm$^{-1}$, using the MCT detector.
159     In March 2016, an EM27/SUN spectrometer was implemented at UNA to continuously measure $XCO_2$,
160 $XCH_4$, $XH_2O$, XCO total columns from solar NIR spectra with a spectral-resolution of 0.5 cm$^{-1}$ (MPD of 1.8 cm).
161 The spectrometer is equipped with its own solar tracker (Bruker CAMTracker; Gisi et al., 2011) capturing and
162 redirecting the solar beam into a RockSolid$^{TM}$ pendulum interferometer equipped with a Quartz beamsplitter. The
163 EM27/SUN, with serial number #62 installed at the UNA station (hereafter EM27-SUN_62), was initially operated
164 with a standard InGaAs-diode detector sensitive to the 5500-11000 cm$^{-1}$ spectral range, to which a second InGaAs
165 detector with Ge filter was added in 2017 for CO measurements through a second channel (4000 – 5500 cm$^{-1}$)
166 (Hase et al., 2016). Further details on the technical characteristics and systematic performance evaluation of the
167 EM27/SUN spectrometer are given in Frey et al., (2019) and Alberti et al., (2022). The spectrometer was installed
168 in a home-made protective box, including a remotely-controlled dome cover, a GPS and a PCE-THB-40 data-

169    logger for precise timing and surface pressure measurements. Double sided forward-backward interferograms are

170    routinely recorded with a scanner velocity of 10 kHz, so that the recording time of one measurement (averaging

171    10 IFGs scans) is close to one minute.

172    Additionally, $CO_2$, CO, $CH_4$ and $H_2O$ surface measurements are continuously performed at the UNA

173    station using a Cavity Ring-Down Spectrometer (CRDS, model G2401 from Picarro Inc.). The CRDS spectrometer

174    uses a laser to quantify the spectral features of gas-phase molecules in an optical cavity offering effectively of up

175    to 20 km absorption path length. Frequency shifts are prevented with a high-precision-wavelength monitor and

176    temperature and pressure are precisely controlled by the analyzer. The quantification is improved by the

177    simultaneous spectral analysis of the measured gases. A calibration system using 3 gas standards provided by the

178    National Oceanic and Atmospheric Administration Earth System Research Laboratory (NOAA ESRL), traceable

179    to the WMO2007 scale, was set up in 2018 at UNA and in 2019 at ALTZ. Data collected before the installation of

180    the calibration systems were corrected with calibration coefficients obtained in 2018. The sampling inlet using

181    Synflex tubing was placed at 24 m a.g.l. at UNA station and includes a Nafion air dryer, as described in detail by

182    González del Castillo et al. (2022). Data are continuously collected at 0.3 Hz rate and their uncertainties, calculated

183    as the standard deviation of raw data over 1-minute intervals when measuring calibration gases, are equal to 0.03

184    ppm at UNA (González del Castillo et al., 2022).

185    Finally, continuous mixed-layer height (MLH) measurements are performed since 2008 at UNA using a

186    CL31 ceilometer instrument (Vaisala). This is a robust commercial instrument which emits light pulses at 10 kHz

187    repeating frequency at 910 nm using an indium-gallium-arsenide diode laser. It detects the backscatters signal

188    through a single lens with a silicon avalanche photodiode. The resulting backscattering profiles have a vertical

189    resolution of 10 m and reach an altitude of 7,500 m. The profiles have been used to retrieve MLH above the city

190    since 2011 (García-Franco et al., 2018).

191    **2.2 The ALTZ background station: Total columns and surface measurements**

192    The Altzomoni Atmospheric Observatory (ALTZ) was equipped with a high-resolution FTIR

193    spectrometer (model IFS120/5HR, Bruker) in 2012, capable of measuring atmospheric spectra in the NIR and MIR

194    spectral regions with 257 cm MPD, equivalent to a spectral resolution of 0.0035 cm$^{-1}$. The instrument is installed

195    into a container with a motorised dome cover on the roof and a microwave communication system (60 km line-of-

196    sight to the university campus), which allows a fully-remote control of the instruments. When the dome is open, a

197    solar tracker (CAMTracker; Gisi et al., 2012) collects the solar beam and orients it toward the spectrometer

198    entrance. The spectrometer can be operated with KBr or $CaF_2$ beam splitters, 3 different detectors (MCT, InSb,

199    and InGaAs) and a set of 7 optical filters is installed in a rotating wheel. The measurement routine consists in the

200    acquisition of high (0.005 cm$^{-1}$), medium (0.02 cm$^{-1}$ and 0.1 cm$^{-1}$) and low (0.5 cm$^{-1}$) resolution spectra in the NIR

201    and MIR spectral ranges using the different NDACC filters (~40 min for a complete sequence).

202    The NIR CO and $CO_2$ spectra (0.02 cm$^{-1}$) used in this study were recorded as the average of two scans

203    taken for approximately 38 s with a scanner speed of 40 kHz. The MIR CO spectra (0.005 cm$^{-1}$) are deduced from

204    the coaddition of 6 scans (<200 s) with a scanner speed of 40 kHz. Due to a spectrometer laser replacement, the

205    IFS120/5HR measurements were interrupted between November 2020 and February 2021 (Table 1). To avoid an

206    important gap in the measurements, an EM27/SUN (EM27/SUN_38) was temporarily installed at the station

during this period. The intercalibration factors used for combining the two types of measurements were determined

from previous side-by-side measurements performed during February 2021 (see Table S1 and section 3.1.3).

A CRDS (model G2401 from Picarro Inc.) instrument was implemented at the station in 2014 providing

continuous $CO_2$, CO, $CH_4$ and $H_2O$ surface measurements (Gonzáles del Castillo et al., 2022). The sampling inlet

using Synflex tubing was placed at 4 m a.g.l. and includes a Nafion air dryer (similar installation to UNA). A

calibration system similar to that implemented at UNA, using 3 NOAA ESRL gas standards, was set up in 2019.

The station also includes meteorological instruments, pressure and temperature sensors and visible cameras among

other instrumentation for atmospheric and environmental monitoring.

**2.3 The VAL station: Total column measurements**

The VAL station, located in Vallejo in the northern part of MCMA, is part of the city's air quality network

(RAMA) run by SEDEMA. An EM27/SUN spectrometer (EM27/SUN_104) was installed at this station in 2019

together with a surface $CO_2$ sensor. The VAL spectrometer has been performing measurements with the two

detectors since November 2019. Additionally, the VAL site included a low-cost medium precision $CO_2$ sensor, as

a part of a network implemented during the MERCI-CO2 campaign. It consists of a NDIR-type of sensor

(SenseAir, model HPP3) that can measure in the 0 to 1000 ppm range and after a calibration and target gas follow-

up procedure, can produce data with <1% accuracy (Porras et al., 2023).

**3.1 FTIR data processing and analysis**

In this study, we used the solar absorption measurements acquired by five different FTIR instruments

(i.e: three EM27/SUN, a Vertex 80 and a IFS120/5HR) to estimate the $XCO_2$, and XCO total columns at each

station. The retrieval strategies were adapted as a function of the spectral resolution and averaging kernel of each

species. Table 2 summarises the different products used in this study, and their retrieval parameters.

*Table 2: FTIR analysis: Description of the different FTIR products, retrieval strategies and parameters used in this study.*

| Instrument (spectral resolution) | Gas | Microwindows (cm$^{-1}$) | Interfering gases | Retrieval code | Retrieval method |
|---|---|---|---|---|---|
| EM27/SUN and IFS-120/5HR LowRes (0.5 cm$^{-1}$) | $CO_2$ | 6173.0 - 6390.0 | $H_2O$, $CH_4$ | PROFFAST | Scaling VMR COCCON strategy |
| | CO | 4208.7 - 4318.8 | $H_2O$, HDO, $CH_4$, HF | | |
| | $O_2$ | 7765.0 - 8005.0 | $H_2O$, $CO_2$, HF | | |
| IFS-120/5HR (0.02 cm$^{-1}$) (TCCON-type) | $CO_2$ | 6180.0 - 6260.0 6310.0 - 6380.0 | $H_2O$, $CH_4$, HDO | PROFFIT9.6 | Scaling VMR |
| | CO | 4208.7 - 4257.3 4262.0 - 4318.8 | $CH_4$, $H_2O$, HDO | | |
| | $O_2$ | 7765.0 - 8005.0 | $H_2O$, $CO_2$ , HF | | |
| IFS-120/5HR (0.005 cm$^{-1}$) (NDACC-type) | CO | 2057.70 - 2058.00 2069.56 - 2069.76 2157.50 - 2159.15 | $O_3$, $N_2O$, $H_2O$, OCS and $CO_2$ | PROFFIT9.6 | Profile NDACC strategy |

| Vertex80 (0.1 cm$^{-1}$) | CO | 2056.70 – 2059.00 2068.56-2069.77 2156.50-2160.15 | O$_3$, N$_2$O, H$_2$O, OCS and CO$_2$ | PROFFIT9.6 | Profile |
|---|---|---|---|---|---|

230

### 3.1.1 EM27/SUN spectra analysis

232 Double-sided interferograms from the EM27/SUN were analysed following the standardised COCCON protocol,
233 using PREPROCESS and PROFFAST codes, developed by the KIT and made freely available (https://www.imk-
234 asf.kit.edu/english/COCCON.php). The codes and retrieval methods are fully described in Sha et al. (2020), Frey
235 et al. (2021) and Alberti (2023) and only briefly summarised here. The PREPROCESS algorithm generates the
236 required spectra by a Fast Fourier Transform. The processing incorporates various quality checks, as a signal
237 threshold, intensity variations during recording, requirement of proper spectral abscissa scaling, and generates
238 spectra only from raw measurements passing all checks (the remaining ones being flagged). We used the ILS
239 parameters (i.e: modulation efficiency amplitude and phase error) reported on the KIT-COCCON website
240 (https://www.imk-asf.kit.edu/english/COCCON.php) and in Alberti et al. (2022), corresponding to the initial KIT
241 calibration of the spectrometers (Frey et al., 2019, Alberti et al., 2022). The PROFFAST-PCXS module (i.e:
242 forward model of PROFFAST) pre-calculates daily lookup tables of the molecular absorption cross-sections
243 according to the meteorological parameters and gas trace VMR profiles priors. The latest PROFFAST-PCXS
244 version uses the HITRAN 2020 spectroscopic linelists (with some extensions, e.g., line mixing parameters added
245 for CH$_4$). Here, we used the standard COCCON linelists as incorporated in the previous PROFFAST version, i.e:
246 HITRAN 2008 for CH$_4$, HITRAN 2012 for CO$_2$, a modified version of HITRAN 2009 by Toon (2014) for H$_2$O, a
247 TCCON standard linelist for O$_2$, and the same solar line list as previously used by TCCON (compiled by G.C.
248 Toon for GGG2014). The least-squares fitting code PROFFAST-INVERS retrieves the total columns by scaling
249 the prior VMR profiles iteratively until adjusting the fit to the measured spectra. The intraday variability of surface
250 pressure is considered in the retrieval, interpolated from the in-situ pressure measurements. For tying the column-
251 averaged abundances provided by COCCON to TCCON data, PROFFAST applies post-process Airmass-
252 Dependent (ADCF) and Independent (AICF) corrections, independent from the instrument, similar as used in the
253 TCCON process (Sha et al., 2020, and Alberti, 2023). The corrections and parameters used are reported in the
254 COCCON website and Alberti, (2023).

255 We automatized and adapted the data processing to obtain a preliminary "real-time" hourly-updated
256 analysis (hereafter, AN1) for each site, additionally to the off-line treatment (hereafter, AN2) applying the standard
257 COCCON procedure. The meteorological data used in the AN1 retrieval were derived from the daily-available
258 radiosonde data, provided by Servicio Meteorologico Nacional (SMN) from measurements performed in the early
259 morning (6 AM LT) at the Mexico City International Airport. The AN1 strategy adopted fixed VMR priors for
260 each species, consisting in the averaged profile of 41 years (1980-2020) run of the Whole Atmospheric Community
261 Climate Model (WACCM), as commonly used in the NDACC community. The AN2 processing, generating the
262 COCCON standard products, used the daily TCCON meteorological data and priors (GGG2014 version of MAPs
263 files), downloaded from the Caltech server, which are based on National Centers for Environmental Prediction
264 (NCEP) reanalysis. For both AN1 and AN2 processing, we used the in situ intraday surface pressure measurements
265 from the PCE-THB-40 sensors. A correction factor was applied to the pressure measurements to take into account

266 the bias between the different pressure sensors used, previously intercompared by a few days of side-by-side

267 measurements.

268 $CO_2$, $O_2$, and CO were analysed in the 6173.0 - 6390.0 $cm^{-1}$, 7765.0 - 8005.0 $cm^{-1}$ and 4208.7 - 4318.8 $cm^{-1}$

269 spectral windows, respectively. The $XCO_2$ and XCO column-averaged dry air mole fractions were calculated

270 using the $O_2$ retrieved total columns, according to Wunch et al. (2009):

271 $$Xgas = 0.2095 \, (C_{gas} \, / \, C_{O2}) \tag{1}$$

272 where $C_{gas}$ and $C_{O2}$ are the target gas and $O_2$ total columns, respectively.

273 The real-time (AN1) and COCCON (AN2) $XCO_2$ and XCO products showed relative differences lower than 0.05%

274 and 5%, respectively. The results presented hereafter are based on the official COCCON products (AN2 analysis).

275 **3.1.2 Vertex80 and IFS120/5HR spectra analysis**

276 High (0.005 $cm^{-1}$) and medium (0.02 $cm^{-1}$ and 0.1 $cm^{-1}$) resolution solar-absorption spectra are processed using

277 the PROFFIT9.6 code (Hase et al., 2004).

278 $XCO_2$ is retrieved from the NIR 0.02 $cm^{-1}$ resolution spectra applying the procedure described in Baylon et al.

279 (2017), in which two independent $CO_2$ and $O_2$ VMR-scaling retrievals are performed using fixed WCCAM VMR

280 priors and NCEP-derived meteorological data. Spectral windows and interfering gases (Table 2) are similar to

281 those used in the standard TCCON procedure. $XCO_2$ is then calculated from the retrieved $CO_2$ and $O_2$ total columns

282 by applying Eq. (1).

283 For the ALTZ analysis, CO was retrieved from the high (0.005 $cm^{-1}$) resolution spectra in the MIR region, applying

284 the standard NDACC procedure (Pougatchev et al., 1994; Rinsland et al. 1998; Table 2). It uses a profile retrieval

285 strategy with fixed WACCM VMR priors and NCEP meteorological data. Since the $O_2$ specie is not analysed in

286 the MIR region, the XCO was determined using the dry air columns ($C_{dryair}$):

287

288 $$XCO = \frac{C_{CO}}{C_{dryair}} \tag{2}$$

289 with:

290 $$C_{dryair} = \left(\frac{P_g}{g} \, m_{dryair}\right) - \left(C_{H2O} \, \frac{m_{H2O}}{m_{dryair}}\right) \tag{3}$$

291
292 where $C_{CO}$ and $C_{H2O}$ are the retrieved CO and $H_2O$ total columns, $g$ the column-averaged gravity acceleration, $P_g$

293 the ground pressure and $m_{dryair}$ and $m_{H2O}$, the dry air and $H_2O$ molecular masses respectively. In addition, we

294 analysed XCO from the NIR spectral region to complement the MIR time-series, occasionally interrupted when

295 the liquid nitrogen was missing at the station. The CO and $O_2$ columns in the NIR region were analysed using

296 scaling retrievals in the same spectral windows as that used by TCCON (Table 2), but with fixed WACCM VMR

297 priors and NCEP meteorological data. XCO was calculated from the CO and $O_2$ retrieved total columns applying

298 Eq. (1). To minimise the air mass dependence effect (likely low for CO), we filtered out data with a SZA >60°.

299 XCO NIR and MIR products were compared and intercalibrated (section 3.1.3).

300 For UNA, we used the XCO total columns calculated from the Vertex80 measurements to complement the

301 EM27/SUN time series during the period when it was operating with a single detector (between March 2016 and

302 September 2017). CO was analysed from the 0.1 $cm^{-1}$ resolution spectra in the MIR spectral range, using a standard

303 NDACC profile retrieval strategy and the PROFFIT9.6 retrieval program with constant WACCM VMR priors and

304 NCEP meteorological data. Spectral windows (Table 2) were adapted following Pougatchev and Rinsland (1995).

305 Previous CO total columns time series retrieved from the same method at UNA were presented in Garcia-Franco

306 et al. (2018) and Borsdorff et al. (2018, 2020). Only the constraint of these CO retrievals were adjusted for the

307 Megacity and allowed in addition a free fitting of the mixing layer concentration, following the work by Stremme

308 et al. (2009) in which low resolution MIR spectra with a different retrieval program have been analysed.

### 3.1.3 Measurement precision and FTIR product intercomparison

310     Side-by-side measurements were performed at the ALTZ and UNA stations on several occasions (Table1)

311 to assess the FTIR measurement precisions, to characterise the bias between the different products and to define

312 the inter-calibration factors for the $XCO_2$ and XCO products. We used the EM27/SUN_62 products as reference,

313 for which we previously applied the standard $XCO_2$ and XCO calibration factors reported in Alberti et al. (2022),

314 to inter-calibrate our results with the COCCON network and the Karlsruhe TCCON station operated by KIT. The

315 linear regression parameters from the different measurement pairs and the calibration factors are presented in the

316 Supplementary data (Table S1 and S2).

317 We found a bias lower than 0.2% and 1.0% between the three EM27/SUN, for $XCO_2$ and XCO respectively, and

318 a coefficient of determination ($R^2$) higher than 0.99.

319 On the other hand, the precision of the EM27/SUN measurements was assessed by calculating the standard

320 deviation over a 5 min-interval period, and found to be on average 2.7 ppb and 0.3 ppm for XCO and $XCO_2$,

321 respectively.

322 The intercomparison of the IFS120/5-HR high resolution (0.02 cm$^{-1}$) products and the EM27/SUN $XCO_2$ products

323 was performed for the daily average data used in this study. The calibration factors were determined using i) the

324 EM27/SUN $XCO_2$ products and ii) the IFS 120/5-HR low resolution (0.5 cm$^{-1}$) product (Fig. S2), processed in the

325 same way as the COCCON EM27/SUN data but having the advantage of being measured even outside the

326 campaigns carried out with the EM27/Sun. We finally found a bias around 0.4% (slope=0.996), and a coefficient

327 of determination $R^2$ of 0.92. This bias is of order of that expected when comparing TCCON and COCCON products

328 (Frey et al., 2019), when no empirical calibration is applied. On the other hand, a bias of 2% (and $R^2$=0.92) was

329 found comparing the XCO from the EM27/SUN and the Vertex (MIR) products at UNA.

330 One of the main contributions of the apparent bias observed when comparing products from different instruments

331 and using different retrieval strategies can be due to their respective Averaging Kernel (AK) which characterise

332 the smoothing error. It is especially the case in the comparison of XCO from the EM27/SUN (i.e: NIR scaling

333 retrieval product, Degree Of Freedom (DOF) =1) and from the Vertex (MIR profile-product, DOF > 2). To assess

334 this effect, we refined the comparison after smoothing the vertically resolved Vertex profiles with the EM27/SUN

335 AK (following Rodgers, 2000; Borsdorff et al., 2014, 2018) and re-calculating the smoothed Vertex total columns.

336 After this smoothing, the bias is reduced to 0.2% instead of 4.1% for the CO total columns. For the XCO product,

337 which includes the use of the surface pressure for the MIR product and the retrieved $O_2$ column for the NIR product

338 the bias is reduced to 0.4% instead of 3.5%.

**3.2 Surface CRDS data analysis**

The surface $CO_2$ and CO data acquired with the CRDS analysers were processed and averaged following the procedure described in González del Castillo et al. (2022). Data were averaged and their standard deviation calculated, per minute, then per hour. To extract the trend and seasonal CO and $CO_2$ variability, data were filtered by discarding hours generally affected by transient and very local effects. Data recorded between 13 and 17h with standard deviations lower than 6.0 ppm were selected for the UNA station, while nighttime data (19 to 5h) with standard deviations lower than 2.0 ppm were selected for the ALTZ station, according to González del Castillo et al. (2022).

**3.3 Mixed Layer height from the Lidar measurements**

The MLH is retrieved using a combined algorithm based on the gradient method and a wavelet-covariance transformation as described in detail by García-Franco et al. (2018). These results were compared with radiosonde data and MLH values derived from surface and vertical column densities of trace gases, and more recently Burgos-Cuevas et al. (2022) used the variance of the vertical velocity from a Doppler Lidar (Wind Cube 100, Leosphere) and compared with the ceilometer results at the same location. These studies show that the ceilometer retrieved MLHs compare well with other techniques during the daytime (they agree within 15% with the trace gas method), which are relevant for this study, whereas late afternoon and nighttime retrieved values might be affected by aerosol residual layers at higher altitudes.

**3.4 Mixed layer CO and $CO_2$ concentrations from FTIR measurements**

Pollutant concentrations within the mixed layer are often estimated using surface measurements, although surface concentrations are very sensitive to the airmass vertical transport, unlike the total columns. It is especially the case within the Mexico City basin where the mixed layer has a strong diurnal dynamics controlling the vertical distribution of the emitted pollutants (Stremme et al., 2009; Garcia-Franco et al., 2018). An estimate of the $CO_2$ and CO vertically averaged concentrations across the mixed layer can be made using the total columns measured at the UNA and ALTZ stations. The dry air mole fraction measured at the UNA station ($XCO_2^{UNA}$) is the weighted mean of that measured in the mixed layer ($CO_2^{ML}$) and in the free troposphere at the ALTZ station ($XCO_2^{ALTZ}$):

$$XCO_2^{UNA} = w_1 \times CO_2^{ML} + w_2 \times XCO_2^{ALTZ}$$

(4)

$$CO_2^{ML} = \frac{XCO_2^{UNA} - w2 \times XCO_2^{ALTZ}}{W1}$$

(5)

The weights (w1 and w2) depend on the pressure difference between the mixed-layer height (MLH) and the UNA station, the pressure on top of the mixed layer is calculated assuming an exponential decay and an effective scale height $H_{scale}$ (assumed to be 8.0 km):

$$w_1 = \left(1 - e^{-\frac{MLH}{Hscale}}\right) \text{ and } w_2 = \left(e^{-\frac{MLH}{Hscale}}\right)$$

(6)

373  The MLH above Mexico City was estimated using the hourly-averaged measurements of the ceilometer at the
374  UNA station. The hourly-averaged $CO_2^{ML}$ and $CO^{ML}$ products were calculated applying the same strategy for the
375  entire time series and are reported in Fig. 7, concurrently to the surface data.

376  **4 Results**

377  The FTIR $XCO_2$ and XCO daily-averaged time series and $CO_2$ and CO surface concentrations obtained at the
378  UNA, VAL and ALTZ stations between November 2015 and June 2021 are shown in Fig. 2. Trends and seasonal
379  variabilities were fitted using a Fourier series analysis (Eq. (7) and black and red solid lines in Fig. 2), following
380  Wunch et al. (2013):

382  $$f(x) = ax + \sum_{k=0}^{n} a_k \cos(2\pi kx) + b_k \sin(2\pi kx), \text{ with n = 2} \qquad (7)$$

384  where $x$ is the time (decimal year), $a$ the mean growth rate (ppm/year), and $a_k$ and $b_k$ the Fourier coefficients
385  modulating the annual cycles. The coefficients for each gas species and station are reported in Table 3.

387  *Table 3: Fourier series fitting parameters for the UNA, VAL and ALTZ $XCO_2$ and XCO time series presented in Fig. 2, and*
388  *calculated from Eq.(7).*

| Fitting parameters (ppm/year) | $XCO_2$, UNA Tot. Col. | $XCO_2$ ALTZ Tot. Col. | $CO_2$ UNA Surface | $CO_2$ ALTZ Surface | XCO UNA Tot. Col. | CO UNA Surface |
|---|---|---|---|---|---|---|
| $a$ | 2.25±0.02 | 2.40±0.01 | 1.6±0.1 | 2.48±0.02 | $(-4.0\pm0.8)\times10^{-3}$ | $(-2.7\pm0.1)\times10^{-2}$ |
| $a1$ | -1.06±0.04 | -0.78±0.04 | 1.7±0.2 | -0.39±0.05 | $(-2.4\pm0.7)\times10^{-3}$ | $(6.5\pm0.4)\times10^{-2}$ |
| $a2$ | 2.11±0.04 | 1.93±0.04 | 1.1±0.2 | -0.36±0.05 | $(-3.2\pm0.8)\times10^{-3}$ | $(1.5\pm0.4)\times10^{-2}$ |
| b1 | 0.71±0.04 | 0.64±0.04 | 2.1±0.2 | 4.62±0.05 | $(8.6\pm0.8)\times10^{-3}$ | $(6.5\pm4.0)\times10^{-3}$ |
| b2 | -0.78±0.04 | -0.45±0.04 | -2.1±0.2 | -1.69±0.05 | $(-7.9\pm0.7)\times10^{-3}$ | $(-2.2\pm0.4)\times10^{-2}$ |

389  **4.1 Trends and interannual variability**

390  The total column $XCO_2$ time series (Fig. 2A) at ALTZ and UNA show a similar mean growth rate around 2.4
391  ppm/year (2.4 and 2.3 ppm/year for ALTZ and UNA, respectively, Table 3) over the whole measurement period.
392  A similar mean growth rate is also found for the surface $CO_2$ time series (Table 3 and Fig. 2 B) in ALTZ (2.5
393  ppm/year). These values are consistent with those estimated at the Mauna Loa Observatory (MLO) reference
394  station for the 2016-2021 period (average of 2.5±0.5 calculated from surface data available in the NOAA site
395  https://gml.noaa.gov/ccgg/trends).
396  At the UNA station a surface mean growth rate of 1.6 ppm/year is found, lower than that observed from the total
397  column measurements. Comparing the surface mean growth rates with those reported by González del Castillo et

al. (2022) for the 2014-2019 period, we observe a significant difference for the UNA station (2.3 ppm/year in González del Castillo et al., 2022) but very similar values for the ALTZ station (2.6 ppm/year in González del Castillo et al., 2022). The difference observed at UNA could stem from (i) starting our new time series at the end
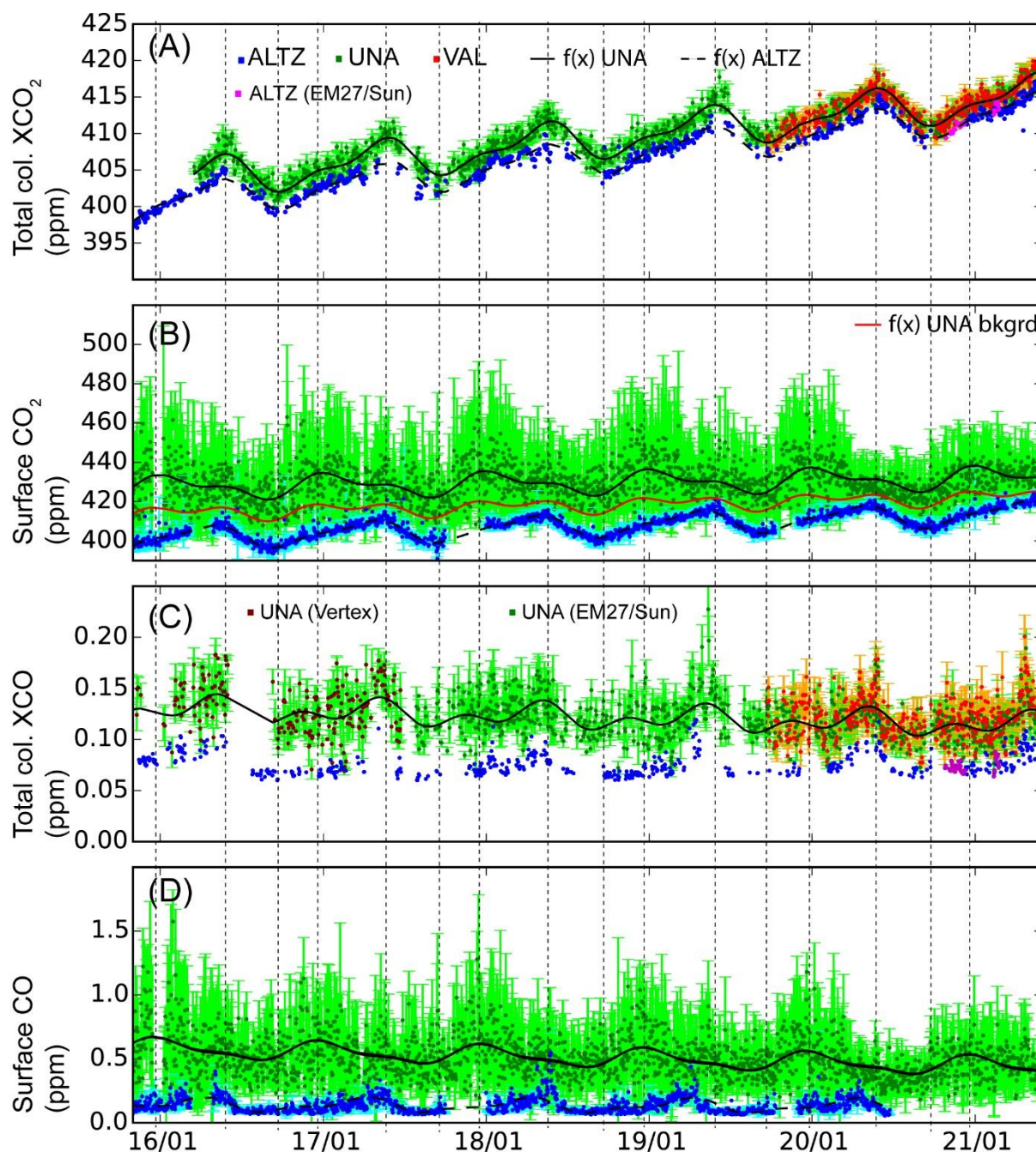
**Figure 2: Time series of (A) the total column $XCO_2$ from the FTIR measurements (B) the $CO_2$ surface concentration from the CRDS measurements, (C) the total column XCO from the FTIR measurements (D) the CO surface concentration from the CRDS measurements for the UNA (in green), VAL (in red) and ALTZ (in blue) stations. For each time series, the daily average data are presented as dots with their daily standard deviations. Black traces show the annual fit calculated from the Fourier series (Eq. (7)). In (A) and (C), we distinguished between ALTZ data obtained from the IFS120/5HR (in blue) and from the EM27/Sun (in magenta) and in (C), between the CO total columns obtained from the VERTEX instrument (in brown) and the EM27/Sun (in green) at the UNA station. In (B) the red curve corresponds to the background fit, calculated following Gonzalez del Castillo et al. (2022), to determine the annual trend and seasonal cycles. Dash lines highlight the minimum and maximum of the annual cycles for the different products.**

412  of 2015, when the annual growth rate is maximum (González del Castillo et al., 2022) and (ii) the inclusion of the

413  2019-2021 period, when the mean growth rate clearly decreased. At the VAL station, the total column $XCO_2$ time

414  series are found very similar to those observed at UNA stations (Fig. 2A). Figure S1 shows that 86% of the daily

415  average data at VAL and UNA have a difference lower than 1.0 ppm, although a large part of the comparison was

416  done during the COVID19 lock-down period (Table1), for which lower gradients are expected due to the decrease

417  of the anthropogenic emissions.

418  The interannual variability can be explored through the time series of the mean annual growth rate (AGR) and the

419  monthly-sampled annual growth rate (MAGR), according to Buchwitz et al. (2018). The MAGR is calculated by

420  month, as the difference between the monthly-average Xgas data of a year $i$ and the monthly-averaged data of the

421  previous year $(i-1)$. The AGR is obtained for each year, averaging all of the MAGR. The AGR and MAGR for

422  total column and surface measurements are presented in Fig. 3. We include data from the MLO in Fig. 3A, for

423  which the AGR (dashed black curve) was derived from the surface data available in the NOAA site.

424  At ALTZ, the interannual variability of the total column $XCO_2$ AGR (Fig. 3A) was found similar to that obtained

425  from both the ALTZ and MLO surface data, with a coincident peak in 2016, reaching an AGR value of 3.5 (surface

426  data) and 4.0 (total column data) ppm/year. Surface data AGR time series show a second peak in 2019, which is

427  not apparent for the total column $XCO_2$ time series. The time series of the MAGR (Fig. 3C) allows better

428  identifying and characterising the period and duration of the anomalies. The 2016 $XCO_2$ anomaly has a duration

429  up to 15 months (from October 2015 to March 2017), reaching a maximum value (around 5.0 ppm/year) between

430  March and July 2016, corresponding to a factor of 2.8 higher than the 2013-2015 base level (1.8 ppm/year).

431

432
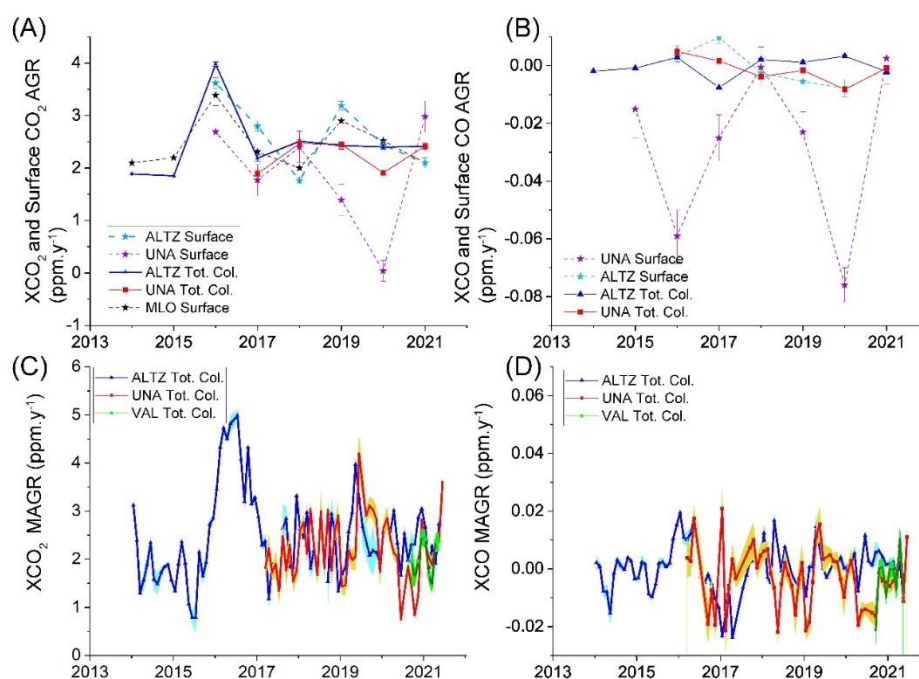
**Figure 3: XCO₂ (A) and XCO (B) annual growth rates (AGR) and XCO₂ (C) and XCO (D) monthly-sampled annual growth rate (MAGR) obtained from total column and surface measurements for UNA, VAL, and ALTZ stations. In (A), the Mauna Loa (MLO) AGR trend was added in black dash-line. In (A) and (B) errors bars represent the standard error after removing annual cycles, reflecting the data sample quality. The standard error for the MAGR is shown as shaded area in (C) and (D).**

At UNA, the $XCO_2$ AGR and MAGR time series (Fig. 3A and 3C) are very similar to those observed at the ALTZ station, except for the year 2020. During this year, the AGR dropped by ~20% at UNA before returning in 2021 to the level of the previous two years. This behaviour contrasts with the AGR observed at ALTZ, which remains nearly constant between 2017 and 2021. The MAGR time series at UNA (Fig. 3C) shows that this drop is dominated by the exceptionally low June and October growth rates, representing the lowest MAGR values of the UNA time series. This observation is supported by the VAL MAGR, although the time series is much shorter. The surface $CO_2$ AGR at UNA shows a much higher interannual variability, with the strongest anomaly observed in 2020, where the AGR is close to zero. A very clear decrease of the day-to-day and intraday $CO_2$ surface variability is observed in Fig. 2B from April to mid-September 2020, consistent with the $XCO_2$ MAGR anomaly.
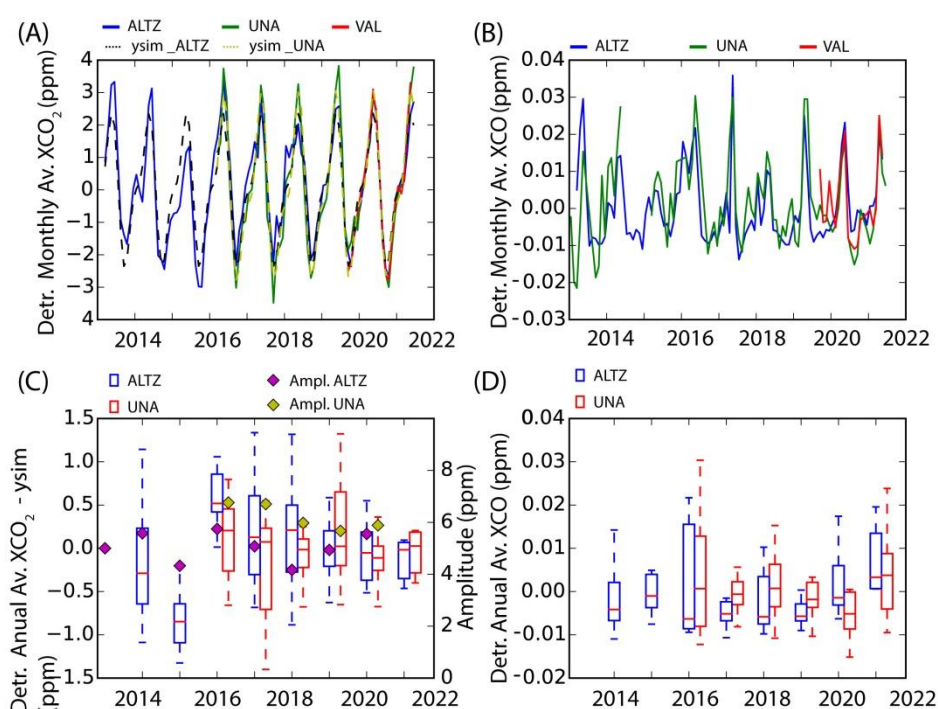
**Figure 4: Interannual and annual variability of the detrended $XCO_2$ and XCO total column data at the UNA, VAL and ALTZ stations. In (C) and (D) the whisker diagrams are calculated from the monthly average detrended data. The amplitude is determined as the max-min values.**

Upon examining CO, the UNA XCO time series (Fig. 2C) has daily averages ranging between 0.10 and 0.23 ppm with a mean and standard deviation of 0.12 and 0.02 ppm, respectively, but shows a decreasing rate (-$4.0 \times 10^{-3}$ ppm/year) over the whole measurement period. The VAL XCO time series show a very similar baseline to UNA, with a daily average difference lower than 0.02 ppm for 85% of the coincident dataset (Fig. S1). At the ALTZ background site, the XCO baseline and day-to-day variability are lower than at UNA and VAL, as expected (mean and standard deviation equal to 0.08 and 0.01 ppm, respectively). The surface CO time series (Fig. 2D) shows a more significant decreasing trend (-$2.68 \times 10^{-2}$ ppm/ year) than the total column data at UNA, while the baseline at ALTZ remains constant around 0.11 ppm. The CO AGR and MAGR at ALTZ and UNA are shown in Fig. 3B and D. Generally, the XCO AGR and MAGR oscillate around their base level at the ALTZ and UNA stations, with short-term anomalies. At ALTZ, a strong negative XCO AGR anomaly is observed in 2017, which was not observed for $XCO_2$, likely resulting from the exceptionally high XCO columns measured during 2016. This is supported by the increase of the XCO MAGR from October 2015 to July 2016 (Fig. 3D), coinciding with

464    the first 10 months of the highest XCO$_2$ anomaly and followed by the lowest XCO MAGR values of the time series

465    (around -0.02 ppm/year in April 2017). At the UNA station, the AGR slightly decreases between 2016 and 2020

466    and increases again in 2021. The most significant and prolonged (>5 months) MAGR anomaly (Fig. 3D) occurred

467    between April and September 2020, with negative values. Some short-term additional anomalies are observed, but

468    only a few of them (in May 2018 and January 2019) are not affected by the limited number of available

469    measurements.

470    **4.2 Seasonal variability and short-term cyclic events**

471    Annual cycles are observed for both total column XCO$_2$ and CO$_2$ surface measurements at ALTZ, UNA and VAL

472    stations (Fig. 2). The maximum and minimum of the total column XCO$_2$ cycles are observed in May-June and

473    September, respectively, with an average amplitude around 5 (ALTZ) and 6 (UNA) ppm.

474    To examine the temporal changes in amplitude and shape of the annual cycles, total column data were monthly-

475    averaged, detrended by subtracting the linear part of the fit ($f(x) = ax$, in Eq. (7)), and compared to the detrended

476    mean annual cycle ($f(x) - ax$) in Fig. 4. To obtain a longer-term view, we included the 2013-2015 period from the

477    ALTZ station, previously published in Baylon et al. (2017), after applying the inter-calibration factors (section

478    3.1.3). At ALTZ, two periods significantly deviated from the average XCO$_2$ seasonal cycle, i.e.: (i) the year 2015,

479    where all the monthly averaged XCO$_2$ are below the fit and with one of the lowest seasonal amplitudes (~4.0 ppm,

480    Fig. 4A and 4C) of the whole time series, and (ii) the year 2016, with higher monthly averages than the mean

481    XCO$_2$ seasonal cycle and the highest amplitude (~5.8 ppm, Fig. 4A and 4C). At UNA, the difference with respect

482    to the average XCO$_2$ seasonal cycle is not significant, except for the year 2020, where all the monthly averages

483    are below the mean annual cycle (Figure 4C). During this period, the UNA and VAL XCO$_2$ monthly-averaged

484    data fit exceptionally well with those of the ALTZ station between March 2020 and March 2021 in terms of shape

485    and amplitude, while the UNA and VAL annual cycle amplitudes are slightly higher than those of ALTZ for the

486    other years.

487    Regarding the CO$_2$ surface data (Fig. 2B), annual cycles are observed with maxima and minima reached mid-

488    December and mid-September, respectively. As also reported in González del Castillo et al. (2022), the maximum

489    occurred during winter, when shallower boundary layer prevails and the summer-autumn minimum can be

490    explained by the dilution of trace gases in a deeper convective boundary layer and more active urban vegetation.

491    XCO peaks every year in April-May at the three stations (Fig. 2C and Fig. 4B) and then shows minimal annual

492    values in August, preceding by 1 month the minimum and maximum values of the XCO$_2$ time series. The April-

493    May maximal annual values, also confirmed by TROPOMI measurements (Borsdorff et al., 2020), coincide with

494    the biomass burning season and the periods during which the mixed layer reaches its maximum altitude (García-

495    Franco et al., 2018). During 2015, the XCO time series show a very low maximum reached in February instead of

496    May (Fig. 4B), contrasting with 2016, where high total column XCO values are reached in January and maintained

497    for a period of at least 5 months. 2016 also corresponds to the year with the highest XCO variability of the time

498    series (Figure 4D). Additionally, in 2018, the XCO annual cycles differ from the other years with lower values

499    and a flat shape during the first semester of the year (January-May).

500    Surface CO data (Fig. 2D) also show periodic increases at the ALTZ station with maxima reached during April-

501    May, coinciding with the maxima observed from total column XCO measurements. They confirm the increase of

502    the CO emissions during the biomass burning season, at least dominant in the ALTZ measurements. However, at

the UNA station, cycles are also observed in the surface data but with a maximum coinciding with that of the $CO_2$ surface data, and lagging behind the XCO total columns. These cycles are likely dominated by other processes affecting both CO and $CO_2$ species such as the mixed layer seasonal dynamic.

**4.3 Intraday variability**

The intraday variability of the total columns and surface data are depicted in Fig. 5 and Fig. 6. Since the ALTZ total column data do not present a significant diurnal pattern (the hourly variability remains lower than the standard error of the time series), they are not presented in these plots.
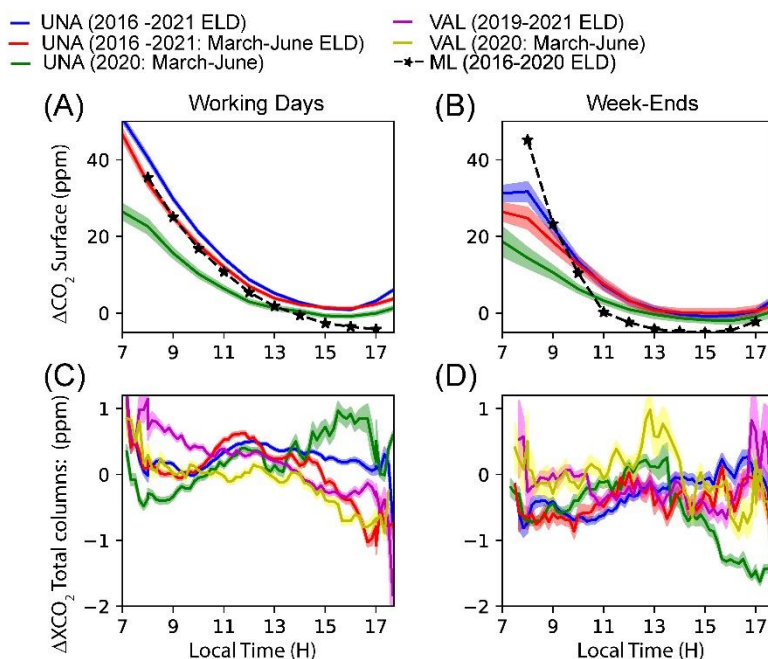
**Figure 5: Diurnal patterns of the detrended surface $CO_2$ mole fractions (A and B) and $XCO_2$ total columns (C and D) measured at UNA and VAL stations. For each panel, the different curves represent different time periods: in blue, the whole measurement period excluding the lock-down period (March-June 2020 ELD), in green the lock-down period (March-June 2020) and in red the whole measurement periods from March to June, excluding the lock-down. The standard errors are presented as shaded areas. Black curves represent the diurnal pattern of $CO_2$ in the Mixed Layer (ML) calculated from the total columns data for the UNA station.**

Total column data were detrended by removing the seasonal fit (black traces in Fig. 2A and Fig. 2C), and averaged over 10 min. To avoid a possible bias due to strong ventilation periods, a filter based on a ventilation index (VI) was applied, following recommendations in Hardy (2001), Su et al. (2018) and Storey and Price (2022). The VI is calculated as the product of average wind speed velocity (between the surface and 100 m height), and the planetary boundary layer height for UNA and VAL locations. The wind velocity and the MLH were estimated with the U and V wind components and the PBL height fields from the hourly ERA5 reanalysis product (Hersbach et al., 2020). In the MCMA, the surface wind speed presents a diurnal pattern, generally reaching a maximum during the afternoon between 14 and 15h LT (Fig. S4). The filter selects the days complying with the following criteria (i) a maximum wind velocity (average 10-100m height) between 10h and 12h LT lower than 1.5 m.s$^{-1}$ (threshold based on Stremme et al., 2013) and (ii) a daily VI lower than 2350 m$^2$.s$^{-1}$, which represents a commonly used threshold for selecting poor ventilation conditions (Hardy, 2001; Storey and Price, 2022). About 60% of the original $XCO_2$ and XCO dataset is selected by applying the filter, and will be considered in the following analysis. We note that about 70% of discarded data corresponds to the January-May period of the year. Filtered total column $XCO_2$ and

530    XCO data were averaged by 10 min and presented in Fig. 5C-D and Fig. 6C-D, distinguishing between the working

531    days (WD) and the week-end (WE) periods. To explore the 2020 lock-down influence on the diurnal pattern, three

532    different periods were distinguished for each plot, the first one (blue trace: 2016 - 2021) corresponding to the

533    whole measurement period excluding the interval between March and June 2020 corresponding to the lock-down

534    period (hereafter, called "ELD" for "excluding the lock down period"), where a significant MAGR decrease was

535    observed; the second (green trace: March- June 2020) only includes the lock-down period, and additionally

536    excludes the rainy season to avoid bias due to incomplete daily time series; and the third period (red trace) is the

537    same as the first one, but only considering the March to June months to be compared with the lock-down period.
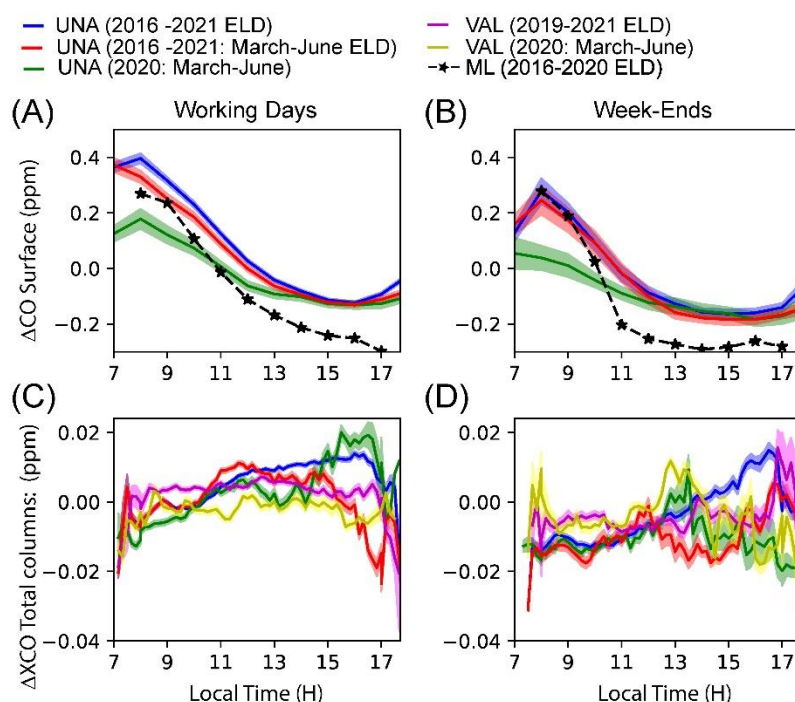
538

539    **Figure 6: Same as Figure 5, but from surface CO and total column XCO measurements.**

540    Surface data from the CRDS analyzers were detrended by removing the background fit following the methodology

541    described in the section 3.2, and filtered to be coincident with the filtered total column measurements (selection of

542    data between 7 and 18 h LT and only including the days with low ventilation conditions). They were finally

543    averaged by hours and presented in Fig. 5A-B and Fig. 6A-B for the WD and WE periods, respectively, for which

544    each curve represents the periods mentioned above.

545

546    The surface $CO_2$ diurnal pattern at UNA station for the whole measurement period (2016-2021, Fig. 5A and 5B in

547    blue) is consistent with the one previously described in Gonzalez del Castillo et al. (2022) for the 2014-2019

548    period, with a maximum observed during the early morning (reached before 7h LT), a minimum during the

549    afternoon (between 15 and 16h LT) and an average amplitude around 45 ppm. A lower amplitude of these cycles

550    is observed at WE (average amplitude of 28 ppm) with respect to the WD periods. During the 2020 lock-down

551    period (green curve), the WD surface $CO_2$ diurnal profile has a comparable amplitude (average amplitude of 26

552    ppm) to those of the WE for the whole measurement period, and slightly higher than that observed during the lock-

553    down WE periods (average amplitude of 22 ppm). The surface CO diurnal profile (Fig. 6: 2016-2021, blue curve)

554    peaks at 8h and then decreases until 16 h LT during any day of the week. The WD and WE data shows amplitudes

555    of up to 0.5 ppm and 0.3 ppm, respectively. During the lock-down period the WD and WE amplitudes are much

556    lower (0.3 and 0.2, respectively), consistently with the $CO_2$ surface observations.

557    The $XCO_2$ and XCO diurnal patterns (Fig. 5C-D and Fig. 6C-D) have very different shapes than those of the surface

558    data, with amplitudes one order of magnitude lower. The variability observed between 7 and 8h is likely due to

559    the low number of measurements during this time interval, and will not be taken into account in the following

560    analysis. The UNA and VAL $XCO_2$ diurnal patterns significantly differ in shape. The VAL WD curve (magenta)

561    continuously decreases from 8h to 17h (amplitude around 2 ppm) during both the whole measurement and lock-

562    down periods, but during the lockdown period, lower values are generally recorded with higher intra-hour

563    variability between 11h and 14h. The general WD decreasing trend suggests a maximum reached during the early

564    morning (before 7h LT). This observation is supported by the $CO_2$ surface measurements performed with the low-

565    cost medium precision $CO_2$ sensors (Porras et al., 2023), recording a maximum between 6h and 7h LT. The UNA

566    $XCO_2$ WD diurnal pattern (blue trace) is almost constant until 10h, then increases until reaching a maximum around

567    12h, slightly decreases until 17h LT and finally shows an abrupt decrease after that. The amplitude of the diurnal

568    variability is around 1 ppm. During the lock-down period, the diurnal profile is different, increasing until 12h LT,

569    slightly decreasing until 13h LT and then increasing again until reaching a maximum at 16h, and finally abruptly

570    decreasing until 17h LT. The lock-down WD $XCO_2$ profile shows lower values than the other periods until 13h,

571    but the peak observed at 16h is not apparent for the other periods. Variability is generally lower at WE (<1ppm),

572    except for the lock-down period, for which an important decrease is observed after 14h LT, but it is likely affected

573    by a low number of measurement days. For XCO, the diurnal profiles also have different shapes at UNA and VAL.

574    At UNA, the March-June XCO diurnal profiles (red and green curves) resemble that of $XCO_2$ for both the lock

575    down and whole measurement periods. When considering the twelve months of the year (blue trace), the maximum

576    curve slightly increases between 12h and 16h, when it reaches its maximum. It contrasts with the variability of the

577    March to June months curves during this time interval, for which an increase is observed during the lock-down

578    period or a decrease if considering the whole measurement period. At VAL, the diurnal profile is fairly constant

579    until 17h with slightly lower values during the lock-down period.

580    The total column XCO diurnal profiles at WE are less reliable with larger standard errors, likely due to the low

581    number of considered measurements. An increase is nevertheless observed at UNA where the considered day's

582    number is statistically more reliable, with a peak around 17h LT, which was not observed for $XCO_2$.

583    The difference observed between the diurnal pattern of the XCO and $XCO_2$ at VAL and UNA is likely due to the

584    different advection drivers in the region mainly controlled by the topography. A Northern surface wind direction

585    (Figure S6) is generally dominating over the Mexican valley but is locally highly influenced by the mountainous

586    barriers. The West-northwest wind component at UNA is likely to be the effect of down-slope flows from the

587    mountain ridge in the early morning (6 – 9 LT mostly), while at VAL, the plateau-to-basin winds are the main

588    influx into the basin coming from the northwest in the morning. There can also be an influence from an up-valley

589    flow in the mornings (de Foy et al., 2006). More generally the VAL station is likely influenced by the north

590    mountain, generating a significant gradient in the CO distribution upwind of the VAL station (Figure 1). In

591    contrast, near the UNA station, the flat ground allows a more efficient mixing and due to the dominant North-

592    Northeast wind component in the late morning, the captured airmasses likely often reflects the MCMA plume

593    emissions.

**4.4 CO and CO₂ within the mixed layer from FTIR and surface data.**

Figure 7 shows the hourly-averaged $CO_2$ and CO concentration within the mixed layer ($CO_2^{ML}$ and $CO^{ML}$ products), calculated from the FTIR measurements (see section 3.4), concurrently to the surface data. The $CO_2^{ML}$ and $CO^{ML}$ products are in agreement with the surface observation, with a slope of 0.95±0.02 ($R^2$=0.74) for $CO_2$ (Fig. 7C) and 0.81±0.02 ($R^2$=0.74) for CO (Fig. 7D). For $CO_2$, the slope was found closer to 1.0 (1.00±0.02) with an offset of -2.9±0.2 and a better $R^2$ (0.77) when discarding the data corresponding to the rainy season. This effect is likely due to the removal of the incomplete daily time series frequently interrupted at the beginning of the afternoon during the rainy season.
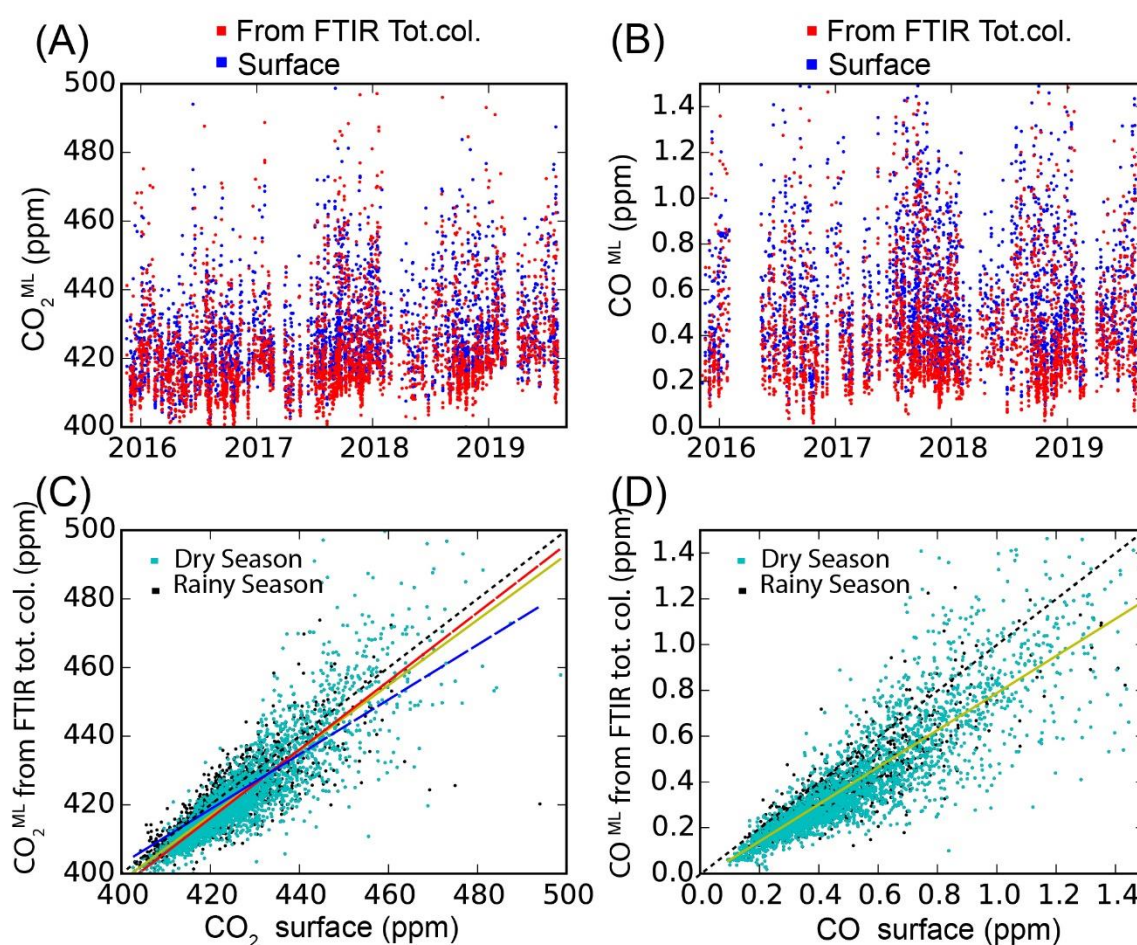
**Figure 7: Comparison between (A) the $CO_2^{ML}$ and (B) $CO^{ML}$ products (red) derived from the ALTZ and UNA total column measurements and the surface measurements at the UNA station (blue). (C) and (D) represent the correlation plots for $CO_2$ and CO, respectively. In (C) and (D), we distinguished between data corresponding to the dry (November to May: cyan) and rainy (June to October: black) seasons. In (C), yellow, red and blue linear regression curves correspond to the whole measurement period (yellow: slope=0.95±0.02; Offset= 17.9±0.2; $R^2$=0.74), the dry season (red: slope=1.00±0.02; Offset: -2.9±0.2; $R^2$=0.77) and the rainy season (blue: slope=0.80±0.03; Offset: 83.7±0.39; $R^2$=0.66). In (D), since no significant difference was found for the different period, the regression line (yellow: slope=0.81±0.02; offset: -0.021±0.004; $R^2$=0.74) represent the whole measurement. The black dash line represents y=x.**

The $CO_2^{ML}$ and $CO^{ML}$ diurnal patterns are presented in Fig. 5 and Fig. 6 (dash lines) together with those of surface measurements, after a similar filtering. The $CO_2^{ML}$ and surface $CO_2$ diurnal patterns (Fig. 5A and 5B) are very similar in shape and amplitude, especially during the WD, although a small difference is observed at the end of

the afternoon (<5 ppm). This difference is likely due to the increase of the uncertainties of the MLH estimate when

it is more diluted. The $CO^{ML}$ and surface CO diurnal profiles (Fig. 6A and 6B) also have similar amplitudes and

shape for both WD and WE, although the $CO^{ML}$ diurnal profile shows lower values (offset around 0.1 ppm at WD).

Despite this very simplified model, these results show that the total column and surface measurements are mutually

very consistent when the seasonal and diurnal variability of the ML expansion above Mexico City is taken into

account.

### 4.5 XCO₂ to XCO enhancements ratios

The XCO and $XCO_2$ correlated enhancements and their ratio can give insights into the combustion efficiency of

the sources in a city, and therefore on their contributions. In this study we explored the variability of the

$XCO/XCO_2$ ratios at both long-term and intraday scales.

For the long-term analysis, the $XCO_2$ "background" level was calculated using a statistical method, using the lower

5th percentile of the measured Xgas over a 1-day running window (You et al., 2021). We did not use the ALTZ

measurements because of (i) the periodic influence of the wildfires in the region during the dry season, and (ii) the

discontinuity of our daily averaged time series. The enhancements above background $\Delta_mXCO_2$ and $\Delta_mXCO$

measured at UNA and averaged by months and their ratios are presented in Fig. 8, as whisker diagrams.
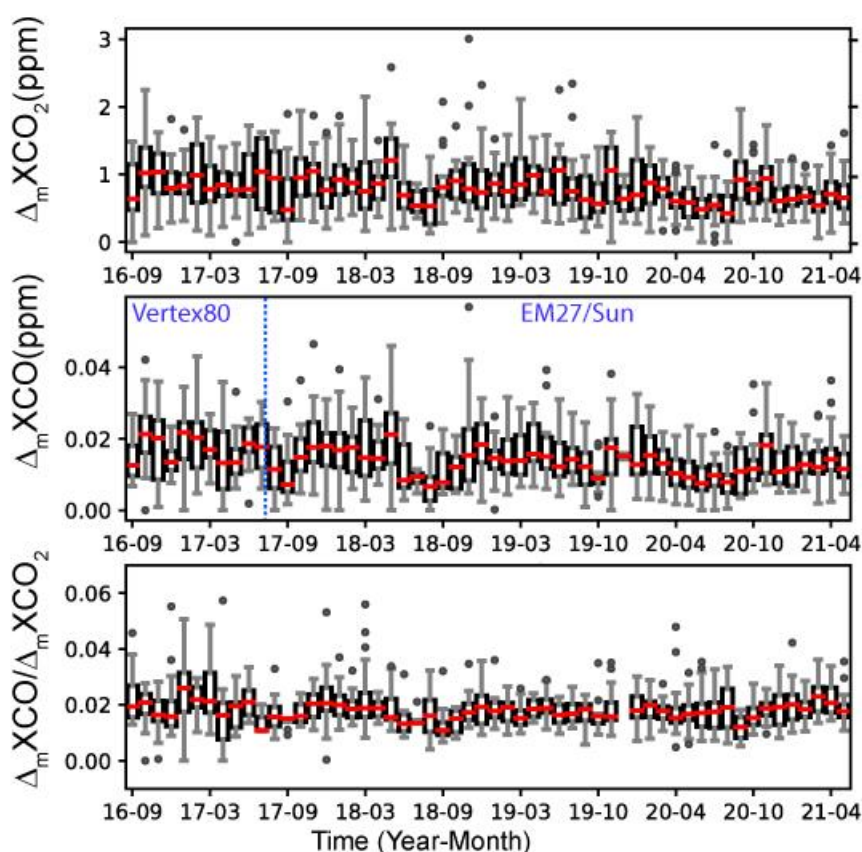
**Figure 8: Whisker diagram representing by month the variability of ΔXCO₂, ΔXCO and their ratio from the UNA measurements.**

Both $\Delta_mXCO_2$ and $\Delta_mXCO$ time series show a slight decrease over time (around 0.05 ppm/year and 0.001

ppm/year, respectively). Although the $\Delta_mXCO/\Delta_mXCO_2$ ratio displays a variability around its mean value

(0.018±0.003), there are no discernible cyclic or long-term trend in the time series, except for the rainy periods of

2017, 2018 and 2020 when low ratios (and low $\Delta_mXCO$ and $\Delta_mXCO_2$ values) were observed. The $\Delta_mXCO$ and

638    $\Delta_m XCO/\Delta_m XCO_2$ ratio show a higher variability at the beginning of the time series (until July 2017) likely due to

639    the use of the CO Vertex products. The long term $\Delta_m XCO$ decrease, also observed in other studies (Garcia-Franco,

640    et al., 2019; Molina, 2021, Hernández-Paniagua et al., 2021) likely reflect the effect of the successive air quality

641    management programs implemented in the CDMX since the 1990s to improve the air quality, including

642    technological advancements and fuel quality enhancements as well as refinery closures, industrial relocation, or

643    fuel substitution. Regarding the low seasonal variability observed for the $CO/CO_2$ ratios, it is likely related to mass

644    burning episodes and high-pressure weather conditions that occur during the dry season.

645    To perform the intraday analysis, the hourly-averaged data were first detrended by subtracting the daily average.

646    The resulting $\Delta XCO_2$ vs. $\Delta XCO$ datasets are plotted in Fig. 9A. The entire $\Delta XCO_2$ and $\Delta XCO$ datasets showed a

647    good correlation at both the UNA and VAL stations, with similar linear regression slopes around $0.0164\pm0.0003$,

648    which is consistent with that found from the surface measurements and the ML product (Fig. 9B). Although there

649    is an actual difference in the emission types of the southern and northern parts of the city, the North hosting

650    industrial and commercial sources and the South being largely residential and commercial, the common and

651    dominant source of CO in the MCMA (at UNA and VAL stations) could incriminate motorised vehicles. The data

652    dispersion around the regression line likely reflects more punctual and local influence of other sources with an

653    important week-to-week variability.

654
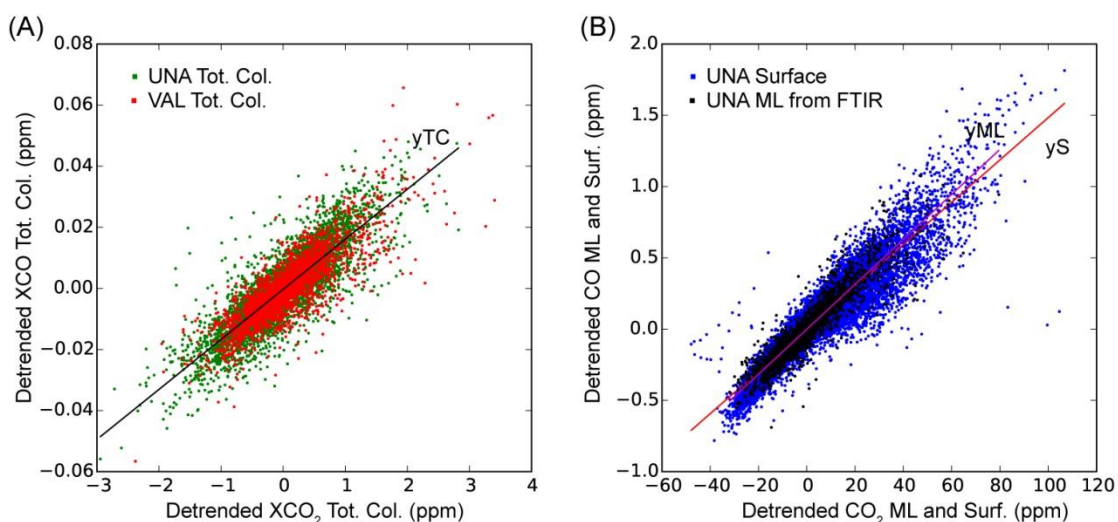
655

656

657    **Figure 9: A: Correlation plot of (A) the detrended (by removing the daily averages) hourly-average total column $XCO_2$**
658    **vs. XCO data, and (B) the detrended hourly average Mixing Layer (ML) and surface $CO_2$ vs. CO products. Solid lines**
659    **represent the linear regression lines, with the following parameters: TC slope=$0.0164\pm0.0003$, $R^2$=0.72 for the total**
660    **columns at UNA and VAL; yS slope=$0.0148\pm0.0001$, $R^2$=0.87 for the surface products and yML slope=$0.0158\pm0.0002$,**
661    **$R^2$=0.88 for the Mixing Layer products.**

662    On the other hand, the total column (UNA-VAL) differences, presented in Fig. S3 can also be used to calculate

663    the $\Delta XCO/\Delta XCO_2$ ratio, with a more precise subtraction of a common background (which assumes a

664    homogeneous background across the entire city) from the two stations. Figure 10 shows the hourly-average $\Delta XCO_2$

665    (UNA-VAL) vs. $\Delta XCO$ (UNA-VAL) correlation plot for the coincident measurement period. A well-defined

666    linear correlation is observed with a slope of $0.015\pm0.001$ and a coefficient of determination of $R^2$=0.80, highly

667    consistent with that found in Fig. 9. The use of the (UNA-VAL) total columns difference notably improved the

668    coefficient of determination, by removing the regional long-term and short-term perturbations affecting the two

669    sites. The intraday variability of the $\Delta$XCO (UNA-VAL)/$\Delta$XCO$_2$ (UNA-VAL) ratio (Fig. 10: colour scale),

670    showing higher columns at VAL during the morning and at UNA during the afternoon likely reflect the North to

671    South transport of air across the city. We note that the ratio remains the same during the lock-down period. We

672    would expect lower intraday (UNA-VAL) $\Delta$XCO and $\Delta$XCO$_2$ amplitudes during the lock-down period, but it is

673    not clearly apparent in this correlation plot.
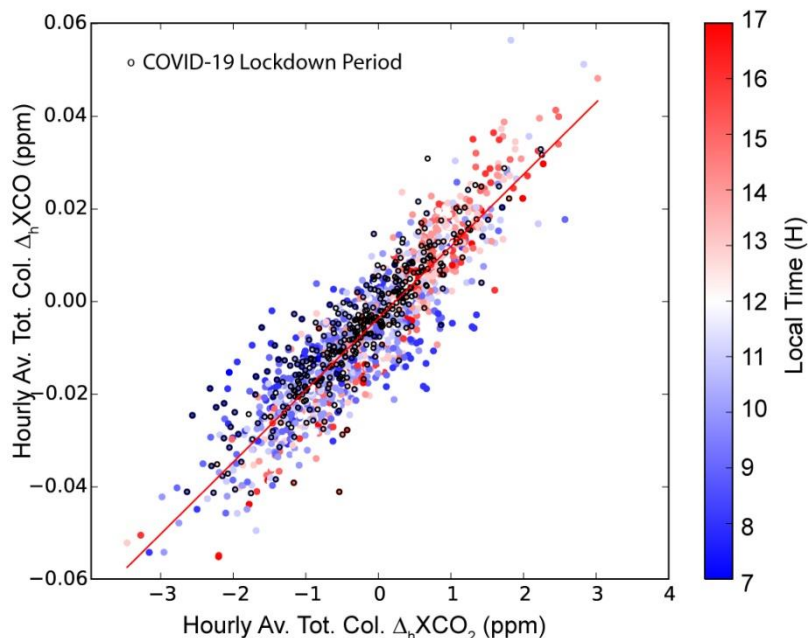
674

675    **Figure 10: Correlation plot of the $\Delta$XCO (UNA - VAL) vs. $\Delta$XCO$_2$ (UNA - VAL) hourly averages (colour scale**
676    **depending on the time is shown to the right) for the coincident measurement period (September 2019 - June 2021). Dots**
677    **with black edges highlight the measurements during the COVID19 lock-down period (March-June 2020). Regression**
678    **line (in red): Slope: 0.015±0.001, R$^2$=0.80.**

679    **4.6 Estimate of CO and CO$_2$ MCMA emissions.**

680    The variability of the long-term CO emissions in the MCMA can be estimated, following the method detailed in

681    Stremme et al. (2013). In that study, they assumed that, since the XCO emissions in the MCMA are mainly due to

682    traffic pollution, the rapid changes observed in the XCO total column (less affected by the airmass vertical

683    distribution) should reflect the CO fresh emissions under certain meteorological conditions. Low ventilation,

684    strong turbulence in the mixed layer and limited zenithal angle of measurements are critical criteria to avoid

685    enhancement due to horizontal transport or local heterogeneity. XCO growth rates can be estimated at specific

686    time intervals complying with these conditions from long-term time series. Further details on the method and

687    estimates of uncertainties due to these assumptions are given in Stremme et al. (2013). Here, we determined an

688    optimised time interval for estimating the mean CO growth rate using (i) the diurnal surface wind speed patterns

689    and (ii) the MLH growth rate, the latter reflecting the turbulence within the  mixed layer (Fig. S4). The time interval

690    complying with a rapid growth of the mixed layer and low surface wind speed (< 2 m.s$^{-1}$) was found between 10

691    and 12h, which is in agreement with the requirements mentioned in Stremme et al. (2013). Growth rates and their

692    uncertainties were determined by year, based on the linear regression (with 95% confidence interval) of the 10-

693    min averaged detrended CO total columns over the 10-12h interval. For example, for the year 2018, we found a

694    CO growth rate of 52±5 kg.km$^{-2}$.h$^{-1}$.

695    To extrapolate the growth rate over the MCMA, we used the TROPOMI CO total column data that we averaged

696    over the 2018-2022 period (Fig. 1), following the same method as described in Stremme et al. (2013). We assume

697    that the total amount of fresh CO is proportional to the total emission of the MCMA and to the total column

698    enhancement at the UNA site, which reflects the CO accumulated at this site. The ratio of the total accumulated

699    CO in the MCMA to the accumulated CO at UNA is therefore the same as the emission ratio of the whole Megacity

700    to the emission flux at UNA. Therefore this ratio is the extrapolation factor and represents an effective area, defined

701    as Eq. (8):

702    $$Eff\_Area = \frac{\int(CO_{MCMA} - CO_{bgrd})}{CO_{UNA} - CO_{bgrd}} \tag{8}$$

703    In Eq. (8), ($CO_{MCMA}$ – $CO_{bgrd}$) is integrated over the area where the CO TROPOMI total columns are higher than

704    a predefined background value. As the TROPOMI overflight time is around 13h30 LT, we cannot neglect the

705    ventilation and slight advection is smoothing out the distribution, so that both the background and the column at

706    UNA have to be chosen carefully. The background column was therefore estimated in two ways (i) from the

707    smallest value observed upwind of the city (cross symbol in Fig. 1) at the elevation of the Mexican basin (contour

708    line separating Mexico City from the Toluca area in the west in Fig. 1) and found to be $1.45 \times 10^{18}$ molec.cm$^{-2}$ and

709    (ii) from the Tecamac site, where the border of MCMA was assumed in Stremme et al. (2013) and where the

710    column was found to be $1.60 \times 10^{18}$ molec.cm$^{-2}$.

711    Due to advection, even locations slightly out of the megacity are presenting enhanced CO columns and it is not

712    clear which is the background column in the Mexican basin. Figure S5 illustrated the sensitivity of the effective

713    area to the background uncertainties. A 10% higher background leads to a 40% smaller extrapolation factor and a

714    40 % emission underestimate. The fresh CO was estimated from the TROPOMI data by removing the background

715    ($1.45 \times 10^{18}$ molec.cm$^{-2}$) to the average total columns found at UNA ($1.93 \times 10^{18}$ molec.cm$^{-2}$) and was found to be

716    $4.79 \times 10^{17}$ molec.cm$^{-2}$. In cases where the CO total column is lower than the background, likely due to the

717    topography effect, we set the difference column to zero for the integration. This topographic effect is important

718    for the considered area, as there are plenty of mountains around the basin, like the mountain ridge in the west

719    (including Ajusco, Desierto de Leones, etc.), some mountains in the mountain ridge on the eastern part of the area

720    including in the south the two volcanoes Popocatépetl and Iztaccihuatl.

721    Finally, we found effective areas of ~2017 km$^2$ (outer area, blue contour line in Fig.1) and ~1178 km$^2$ (inner area,

722    red contour line in Fig.1) considering the two background values given above. The "inner area" reflects conditions

723    without ventilation effect, therefore the outer area is more appropriate for the emission estimates given that the

724    TROPOMI measurements occurred at 13:30 when the ventilation cannot be neglected. The other estimates

725    calculated from the inner area will be thereafter only indicated within brackets and considered to estimate the

726    sensitivity of the result.

727    Since the measured growth rate corresponds to a time interval of only 2 hours in the middle of the day, the CO

728    intraday fluctuations have to be taken into account. Stremme et al. (2013) used a factor which was taken from the

729    available bottom-up inventories and described that the CO emissions per/day are roughly 18.5 times the emission

730    per hour at noon. Assuming the same factor, we estimate a CO rate around 0.71±0.06 (0.42±0.04) Tg/year for

731    2018. If no information about the diurnal distribution of the emission rate is available, we should assume a uniform

732    distribution and an upper value of the CO rate could be estimated using an intraday time interpolation factor of 24

hours instead of 18.5, finally resulting in ~30% higher estimates. Despite the significant uncertainties introduced by spatial and temporal interpolation, their impact on the relative variability, trends and anomalies of the emission rates is less important if the same method and assumptions are consistently applied across the entire time series. $CO_2$ emissions could not be directly estimated using the same method, given its complex diurnal pattern, which is a cumulative result of both natural and anthropogenic contributions and likely been influenced by additional factors, related to instrumental and retrieval effects (i.e: airmass dependence error with a sub-percentage contribution for $CO_2$, non-ideal column sensitivity of the retrieval which represent near 25% overestimation for $CO_2$ anomaly and 5% underestimation for CO anomaly in the PBL). Instead, we based our $CO_2$ estimates on the measured $XCO/XCO_2$ ratio. The average $XCO/XCO_2$ molec. ratio (0.0164±0.0003) determined from the UNA and VAL total column measurement (Fig. 9) was converted to a mass ratio (multiplying it by the molecular weight ratio) and found to be 0.0100±0.0002. Considering this ratio, we estimated the $CO_2$ annual emission at 71±6 (42±4) Tg/year for 2018. Our estimates of CO and $CO_2$ emissions by year and their average over the whole time series, applying the same method, are presented in Fig. 11 and Table S3, concurrently with the SEDEMA inventories for the MCMA. We obtained a 2016-2021 CO and $CO_2$ average emissions of 0.55±0.02 (0.32±0.01) and 46±2 (32±1) Tg/year, respectively, when excluding the lockdown period (Table S3). Here, the given uncertainties are solely those stemming from the propagation of errors in growth rate estimates. Uncertainties on absolute values are much higher when considering spatial and temporal extrapolations errors, but they do not influence the interpretation of relative values.
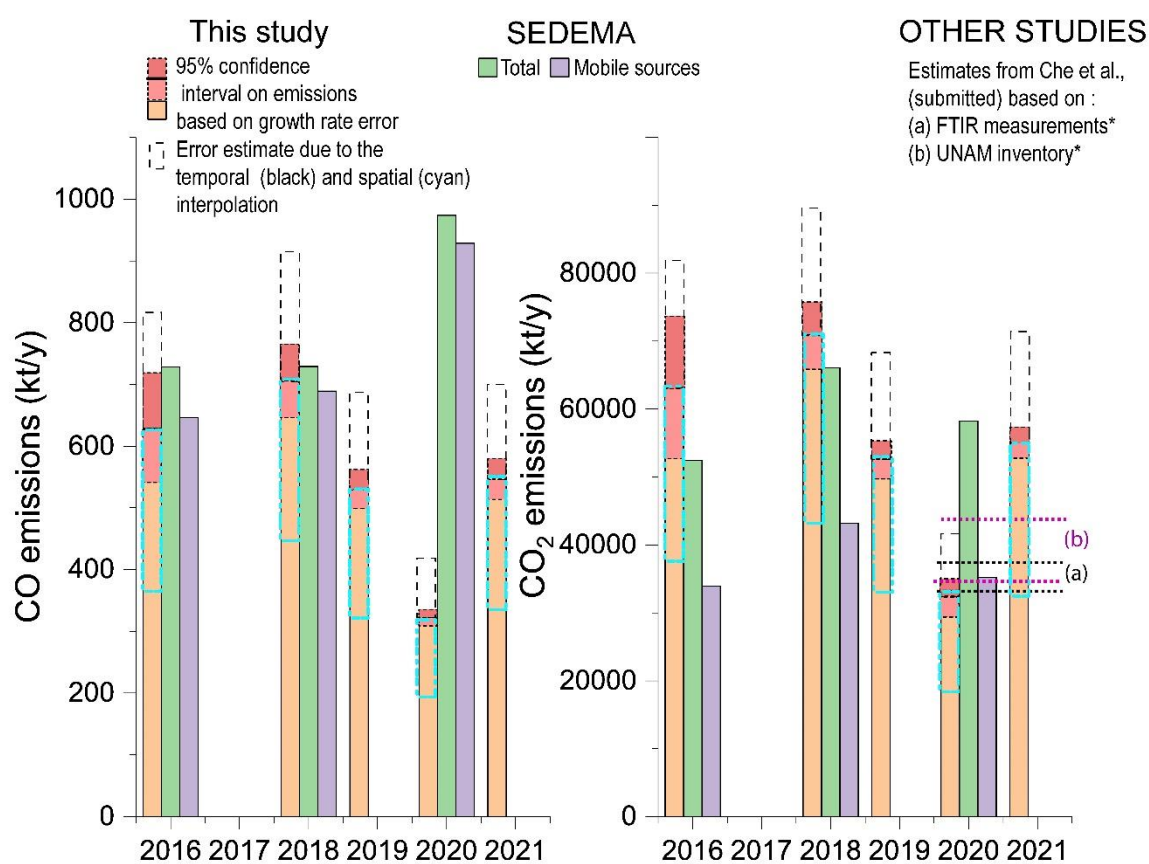
*: The same intraday temporal interpolation factor was applied for the comparison. (a) and (b) were based on the 10/2020 - 05/2021 period

*Figure 11: Comparison of CO and CO2 emission estimations from UNA FTIR diurnal growth rates and from SEDEMA inventories. For CO2 (right), the estimates from Che et al. (submitted) are also reported, although it was based on the 10/2020 to 05/2021 period, after applying the same intraday temporal factor as used for our study to convert the Gg/hour to kt/year.*

**5 Discussion**

**5.1 Long term variability**

755 In this contribution, we characterised the seasonal and inter-annual variability and trends of the CO and $CO_2$ total

756 column and surface concentrations from two urban and one background stations. The average total column 2013-

757 2019 growth rate obtained at ALTZ (~2.5 ppm/year) and its inter-annual variability are in accordance with that

758 typical of the Northern Hemisphere measurements from TCCON stations (hereafter, NH-TCCON) (Sussman et

759 al., 2020: AGR of 2.4 ppm/year for the 2012-2019 period).

762 Both the NH-TCCON and ALTZ stations captured an important increase of the AGR in 2016 (+1.1 ppm/year for

763 the TCCON stations and +2.1 ppm/year for the ALTZ station with respect to 2015), coinciding with the most

764 intense ENSO (El Niño Southern Oscillation) event since the 1950s'. The impact of "El Niño" events on the carbon

765 cycle is not yet fully understood, although they are consistently accompanied by a global increase of $XCO_2$ due to

766 increasing drought in many regions and a decrease in global land carbon uptake. In 2016, an increase of 1.3

767 ppm/year was observed in the Mauna Loa in situ AGR with respect to 2015 (Betts et al., 2018), for which the

768 contribution of the 'El Niño' event was estimated at about 25%, the rest ascribed to an increase of the

769 anthropogenic emissions. In Mexico, the "El Niño" events are generally associated with a decrease in

770 precipitations, with deficits which can reach up to 250 mm in the South-Western area of the country, causing

771 drought and a higher occurrence of wild and forest fires (Bravo-Cabrera et al., 2018, González del Castillo et al.,

772 2020). Our observations from the ALTZ measurements highlight a much higher $XCO_2$ increase (+2.1 ppm/year)

773 during 2016 with respect to 2015 than that observed at the NH-TCCON stations. During this period a small increase

774 in the XCO MAGR (~ +0.02 ppm) is also observed at both ALTZ and UNA stations, maintaining the highest

775 values of the whole time series over more than 4 months. Assuming that the CO MAGR variability captured at the

776 ALTZ station during 2016 rather reflects a change in the global MCMA's emissions, we attempt to delineate the

777 global and local contributions in the 2016 $XCO_2$ ALTZ AGR increase. Adopting a molecular $CO/CO_2$ ratio of ~

778 0.016, a hypothetical increase of the $XCO_2$ MAGR over the 09/2015 - 09/2016 period due to the local emissions

779 would be around +1.2 ppm/year, thus about 60% of the observed increasing rate during this period (+2.1 ppm/year).

780 This gross estimate suggests that the El Niño regional effect only contributed at about 25% (0.9 ppm) to the

781 observed AGR increase, which is close to the estimate from the NH-TCCON stations (~ +1.1 ppm) and from in

782 situ data.

783 On the other hand, our long-term FTIR and surface time series allows examining the effect of the COVID-19 lock-

784 down on the tropospheric $CO_2$ and CO concentration above the MCMA at local and regional scales. The reduction

785 of the surface CO and $CO_2$ AGR at UNA ($CO_2$ AGR to a value close to zero, and CO AGR ~ -0.1 ppm/year) with

786 respect to the other years (Fig. 3), and the strong diminution of their amplitude in the mean diurnal cycles clearly

787 reflect a significant decrease of the local emissions near the UNA station, likely due to a drastic reduction of the

788 urban traffic (the average annual congestion level decreased from 52% in 2019 to 36% in 2020 in Mexico City,

789 from TomTom available estimates https://www.tomtom.com/traffic-index/mexico-city-traffic/).

790 The FTIR total column $XCO_2$ and XCO time series at UNA did not capture such a drastic change, only a small

791 punctual decrease of the MAGR lower than the standard deviation of the whole time series was observed between

792 April and October 2020. These results are in accordance with previous studies in other parts of the world. Although

793 a reduction of 8.8% of the global $CO_2$ emissions was observed during the first five months of 2020 (Liu et al.,

794 2020; Jones et al., 2020) and an annual reduction from 4 to 7% (Le Quéré et al., 2020), the atmospheric total

795 column XCO$_2$ showed a less clear effect (Sussman et al., 2020).

**5.2 CO/CO$_2$ ratio and MCMA emission estimates**

797 In this study, we robustly determined the CO/CO$_2$ ratio characterising the combustion efficiency of the city

798 (0.016±0.01) from both surface and total column measurements at two urban stations. We found the same ratio for

799 the UNA and VAL stations, and this ratio is very consistent with that found using the (UNA-VAL) gradients and

800 using the surface measurements. This ratio is also consistent with that reported by MacDonald et al. (2023),

801 calculated from TROPOMI and OCO-2/3 measurements (0.019) and slightly higher than that obtained from the

802 EDGAR, FFDAS and ODIAC inventories (ratio ~0.012) reported in the same study.

803 Our estimate of CO emissions from the UNA measurements is based on a simplified approach, limited to

804 days with low ventilation and time intervals corresponding to the late morning hours. It assumes a homogeneous

805 area in the footprint and averages selected days without discrimination. Given that the temporal and spatial

806 extrapolation introduces large uncertainties, only the relative and interannual behaviour of the emission can be

807 discussed here, but the approach demonstrates how close column growth rate can be related to emission flux, if

808 meteorological conditions allow neglecting advection. Our estimated range of CO emissions are consistent with

809 the SEDEMA inventories at least for the year 2016 (factor 0.98) and 2018 (factor 1.04) if considering that they are

810 dominated by the mobile sources. However, it is not the case for 2020, for which our estimate is much lower than

811 SEDEMA by a factor of 0.3. During the lock-down period we estimated a decrease of about 55% compared to

812 2018 while in the SEDEMA report, 2020 is the year with the maximum CO emissions (increase of 35% compared

813 to 2018 considering the mobile sources). Both of these estimates contrast with Kutralam-Muniasamy et al. (2021),

814 which reported an increase of 1.1% during the lock-down using the RAMA surface data. The large difference

815 observed between these different studies can be due to i) the different methods used for extrapolating in space and

816 time the emissions, ii) higher uncertainties of the FTIR-based estimates due to an important reduction the selected

817 days of measurements and iii) an over-estimation of the SEDEMA inventory due to a lack of data during the lock-

818 down period. Our estimate is based on the extrapolation of data from only one station (UNA), for which the

819 dominant source is mainly the UNAM traffic activity. During the lockdown, the UNAM was closed and a

820 significant reduction of the local traffic was recorded, but this traffic reduction was likely not representative of the

821 whole MCMA. However, the decrease of the MAGR at both VAL and UNA stations does not support the increase

822 of the CO emissions estimated by the SEDEMA inventory. Interestingly, it was not possible to apply the same

823 method to calculate CO emissions at VAL because the average growth rate was close to zero (Fig. 6). This

824 behaviour at VAL is likely due to the fast dispersion of the pollutant at this site, weakening the link between the

825 diurnal pattern and the emissions.

826 Regarding CO$_2$, our estimates also agree with the SEDEMA's inventory, especially if we consider the total

827 emissions instead of mobile sources (factor of 1.2 and 1.1) for the years 2016 and 2018. For 2020, we estimated a

828 decrease of 55% while the SEDEMA inventory indicates a decrease of about 10%. The CO/CO$_2$ ratios calculated

829 from the SEDEMA data for total emissions are similar to ours (0.014 and 0.011 in 2016 and 2018, respectively),

830 suggesting that our average CO/CO$_2$ ratio is actually representative of the global mixing of the different sources

831 of the MCMA, and not only dominated by the road traffic. Interestingly, according to the SEDEMA inventory,

832 road traffic, the main anthropogenic CO source is identified by ratios (0.019 and 0.016 in 2016 and 2018,

833    respectively) only slightly higher than our global average; whilst the industrial and domestic burning sectors, which

834    represent the second main $CO_2$ anthropogenic sources, produces a one order of magnitude lower ratio. In any case,

835    our measurements are well representative of the main source of the CO and $CO_2$ anthropogenic emissions. Indeed,

836    if we consider the 2018 SEDEMA ratio for mobile sources (0.016), we find $CO_2$ emissions of the order of 43,100

837    kt/year for this year, within ~5% of the SEDEMA estimates.

838    Our results were also compared with the estimates reported in Che et al. (submitted), based on an intensive FTIR

839    measurement campaign performed during the 10/2020 to 05/2021 period and using a Column-Stochastic Time-

840    Inverted Lagrangian Transport model (X-STILT) and a bayesian inversion (Fig. 11). Considering the same

841    measurement period, our method leads to $CO_2$ emission estimates ranging between 29,000 and 49,800 kt/year

842    using inner and outer effective area, respectively, which is consistent with the estimates obtained in Che et al.

843    (submitted), ranging between 32,700 and 37,200 kt/year when applying the same intraday temporal extrapolation

844    factor. Although the method we used for estimating the MCMA emissions is coarse and contains large

845    uncertainties, mainly due to the temporal and space extrapolation, it shows the ability to use one station capturing

846    the variability of the anthropogenic emissions of the MCMA and providing a year-by-year follow-up emission

847    information without using complex dispersion models.

848    **6 Summary and conclusion**

849    We have analysed the variability of the total column XCO and $XCO_2$ above the MCMA from two urban and one

850    background stations. The long-term $XCO_2$ data at the ALTZ station shows an average annual growth rate of ~2.5

851    ppm/year, similar to what has been reported from TCCON stations in the northern hemisphere, and captured the

852    perturbation driven by the 2015-2016 El Niño event. The urban stations show a similar growth rate (~2.3 ppm/year)

853    and unlike at ALTZ, a slight decrease of $XCO_2$ and XCO during the COVID19 lock-down period could be

854    observed. The $CO_2$ and CO concentrations within the mixed layer, estimated from the FTIR total column

855    measurements and ceilometer data, were found to be consistent with the surface measurements. These findings

856    confirm that the concentrations near the surface are mainly controlled by the emissions and the daily behaviour of

857    the mixed layer in MCMA. Our long-term total column and surface time series from both urban stations allowed

858    us to determine with great confidence an average $CO/CO_2$ ratio, indicative of the Mexico City combustion

859    efficiency. The $CO/CO_2$ ratio over our long-term measurement period seems to be fairly constant and equals

860    ~0.016 (mass ratio: 0.010). This value is consistent with other studies such as from satellite measurements (OCO-

861    2/3 and TROPOMI) and the bottom-up inventories reported by MacDonald et al. (2023). Finally, we estimated the

862    CO emissions using the average daily growth rate determined from measurements at the UNA station. Although

863    this method likely leads to an under-estimate of the emissions due to the non-negligible effects of advection, our

864    results were found to be very consistent with the 2016 and 2018 SEDEMA inventories. The same strategy could

865    not be applied at the VAL station, likely because of dominant southward advection of the airmass, due to the

866    complex topography in this part of the MCMA. In contrast, the UNA station is located in a flat ground downwind

867    of the main anthropogenic source of the MCMA which likely allows establishing a direct relationship between the

868    columnar measurements and the MCMA CO and $CO_2$ emissions. We finally estimated the $CO_2$ emissions using

869    the CO growth rate and the $CO/CO_2$ ratio. The finding that our $CO_2$ emission estimates are within 20% of those of

870    SEDEMA for total emissions show that our ratio reflects not only the traffic sources but is also affected by other

871    sources such as industrial activities and domestic burning. The UNA station, with its advantageous orography, is

872 therefore a good site to capture well-mixed emissions from the city and serves as a site to follow the interannual
873 variability and trends of the emissions in this urban environment. Finally, this study showed the feasibility to
874 monitor the long-term evolution of anthropogenic $CO_2$ and CO emissions in Mexico City by deploying only a few
875 EM27/SUN instruments. The methodology employed here for monitoring the long-term temporal variability of
876 CO emission fluxes is likely to be adapted to other urban areas where the topography damps the ventilation down
877 for several hours each day, thereby establishing that the column growth rate is dominated by the emission flux.
878 Although the straightforward model presented here is not intended to replace a complex transport/chemical model
879 for a precise estimate of city emissions, the results obtained demonstrate that it is nevertheless possible to track
880 their temporal evolution with a high degree of reliability.

**7 Author contribution**

882 All the co-authors contributed in the discussion of concepts, and to the preparation of the manuscript. NT, WS and
883 MG were responsible of FTIR measurements and the data analysis. MG and WS lead the ALTZ station
884 development and its long-term operation. AB and EGC were responsible of the maintenance of the instruments at
885 the Altzomoni station. VA helped to classify the days and hours with low ventilation and strong turbulence and
886 provided the UNAM emission inventory. EGC was in charge of the in-situ measurements, with the support of OL.
887 MG and MR led the MERCI-CO2 project. FH lead at KIT the German-Mexican collaboration for the deployment
888 of the high resolution FTIR spectrometer and supports its long-term operation as part of NDACC. FH has helped
889 in the design and setup of the spectrometer and solar tracker before it was shipped to Mexico. He has developed
890 the retrieval code PROFFIT and gives continuously support to the UNAM group for its use and in operating the
891 spectrometer. FH and CA lead the German-Mexican collaboration and give precious help for the EM27/Sun
892 measurements in the frame of the COCCON network. All the co-authors contributed of the writing of the
893 manuscript.

**8 Competing interests**

895 The authors declare that they have no conflict of interest.

**9 Acknowledgements**

897 We thank the two reviewers for their very constructive comments, which help to significantly improve the
898 manuscript. We acknowledge the CONACyT-ANR project 290589 'Mexico City's Regional Carbon Impacts'
899 (ANR-17-CE04-0013-01) for funding. Also the former projects CONACYT 239618 "El estudio del ciclo de
900 Carbono y de los gases de efecto invernadero utilizando espectroscopia de absorción solar" and UNAM-DGAPA
901 PAPIIT IN111521/IN106024 are acknowledged. We acknowledge the CONACyT-ANR project 290589 'Mexico
902 City's Regional Carbon Impacts' (ANR-17-CE04-0013-01) for funding. We acknowledge the technical assistance
903 provided by Omar López, Alfredo Rodriguez, Miguel Robles, Delibes Flores, and the Instituto de Ciencias de la
904 Atmósfera y del Cambio Climatico (UNAM) for the institutional support to carry out this study. We thank T.
905 Blumenstock from the KIT for his precious help and fruitful discussion during the last years. We thank Dr. Thomas
906 Boulesteix for his help at the Altzomoni site, his fruitful discussions.

907

**10 References**

908

909 Alberti Arroyo, C. A.: Ground based FTIR and MAX-DOAS observations of greenhouse and trace gas
910 emissions in the Rhine valley (Germany), St. Petersburg and Yekaterinburg (Russia), Karlsruher Institut für
911 Technologie (KIT), https://doi.org/10.5445/IR/1000162056/v2, 2023.
912 Alberti, C., Hase, F., Frey, M., Dubravica, D., Blumenstock, T., Dehn, A., Castracane, P., Surawicz, G., Harig,
913 R., Baier, B. C., Bès, C., Bi, J., Boesch, H., Butz, A., Cai, Z., Chen, J., Crowell, S. M., Deutscher, N. M., Ene, D.,
914 Franklin, J. E., García, O., Griffith, D., Grouiez, B., Grutter, M., Hamdouni, A., Houweling, S., Humpage, N.,
915 Jacobs, N., Jeong, S., Joly, L., Jones, N. B., Jouglet, D., Kivi, R., Kleinschek, R., Lopez, M., Medeiros, D. J.,
916 Morino, I., Mostafavipak, N., Müller, A., Ohyama, H., Palmer, P. I., Pathakoti, M., Pollard, D. F., Raffalski, U.,
917 Ramonet, M., Ramsay, R., Sha, M. K., Shiomi, K., Simpson, W., Stremme, W., Sun, Y., Tanimoto, H., Té, Y.,
918 Tsidu, G. M., Velazco, V. A., Vogel, F., Watanabe, M., Wei, C., Wunch, D., Yamasoe, M., Zhang, L., and Orphal,
919 J.: Improved calibration procedures for the EM27/SUN spectrometers of the COllaborative Carbon Column
920 Observing Network (COCCON), Atmospheric Measurement Techniques, 15, 2433–2463,
921 https://doi.org/10.5194/amt-15-2433-2022, 2022.
922 Babenhauserheide, A., Hase, F., and Morino, I.: The Fossil Fuel Emissions of Tokyo estimated directly from
923 measurements of the Tsukuba TCCON site, Gases/Remote Sensing/Data Processing and Information Retrieval,
924 https://doi.org/10.5194/amt-2018-224, 2018.
925 Baylon, J. L., Stremme, W., Grutter, M., Hase, F., and Blumenstock, T.: Background
926 $CO_2$ levels and error analysis from ground-based solar absorption IR measurements in
927 central Mexico, Atmos. Meas. Tech., 10, 2425–2434, https://doi.org/10.5194/amt-10-2425-2017, 2017.
928 Betts, R. A., Jones, C. D., Knight, Jeff. R., Keeling, Ralph. F., Kennedy, John. J., Wiltshire, A. J., Andrew, R.
929 M., and Aragão, L. E. O. C.: A successful prediction of the record $CO_2$ rise associated with the 2015/2016 El
930 Niño, Phil. Trans. R. Soc. B, 373, 20170301, https://doi.org/10.1098/rstb.2017.0301, 2018.
931 Bezanilla, A., Krüger, A., Stremme, W., and Grutter, M.: Solar absorption infrared spectroscopic
932 measurements over Mexico City: Methane enhancements, Atmósfera, 27, 173–183,
933 https://doi.org/10.1016/S0187-6236(14)71108-7, 2014.
934 Borsdorff, T., Hasekamp, O. P., Wassmann, A., and Landgraf, J.: Insights into Tikhonov regularization:
935 application to trace gas column retrieval and the efficient calculation of total column averaging kernels, Atmos.
936 Meas. Tech., 7, 523–535, https://doi.org/10.5194/amt-7-523-2014, 2014.
937 Borsdorff, T., Aan de Brugh, J., Hu, H., Aben, I., Hasekamp, O., and Landgraf, J.: Measuring Carbon
938 Monoxide With TROPOMI: First Results and a Comparison With ECMWF-IFS Analysis Data, Geophysical
939 Research Letters, 45, 2826–2832, https://doi.org/10.1002/2018GL077045, 2018.
940 Borsdorff, T., García Reynoso, A., Maldonado, G., Mar-Morales, B., Stremme, W., Grutter, M., and Landgraf,
941 J.: Monitoring CO emissions of the metropolis Mexico City using TROPOMI CO observations, Atmos. Chem.
942 Phys., 20, 15761–15774, https://doi.org/10.5194/acp-20-15761-2020, 2020.
943 Bravo Cabrera, J. L., Azpra Romero, E., Rodriguez Gonzalez, F. J., and Rodriguez López, O.: Effects of ENSO
944 on precipitation in Mexico City, Investigaciones Geográficas, https://doi.org/10.14350/rig.59679, 2018.
945 Buchwitz, M., Reuter, M., Schneising, O., Noël, S., Gier, B., Bovensmann, H., Burrows, J. P., Boesch, H.,
946 Anand, J., Parker, R. J., Somkuti, P., Detmers, R. G., Hasekamp, O. P., Aben, I., Butz, A., Kuze, A., Suto, H.,
947 Yoshida, Y., Crisp, D., and O'Dell, C.: Computation and analysis of atmospheric carbon dioxide annual mean
948 growth rates from satellite observations during 2003–2016, Atmos. Chem. Phys., 18, 17355–17370,
949 https://doi.org/10.5194/acp-18-17355-2018, 2018.
950 Burgos-Cuevas, A., Magaldi, A., Adams, D. K., Grutter, M., García Franco, J. L., and Ruiz-Angulo, A.:
951 Boundary Layer Height Characteristics in Mexico City from Two Remote Sensing Techniques, Boundary-Layer
952 Meteorol, 186, 287–304, https://doi.org/10.1007/s10546-022-00759-w, 2023.
953 Che, K., Cai, Z., Liu, Y., Wu, L., Yang, D., Chen, Y., Meng, X., Zhou, M., Wang, J., Yao, L., and Wang, P.:
954 Lagrangian inversion of anthropogenic $CO_2$ emissions from Beijing using differential column measurements,
955 Environ. Res. Lett., 17, 075001, https://doi.org/10.1088/1748-9326/ac7477, 2022.
956 Che, K., Lauvaux, T., Taquet, N., Stremme, W., Xu, Y., Alberti, C., Lopez, M., García-Reynoso, A., Ciais, P.,
957 Liu,Y., Ramonet, M., Grutter, M. (2024). CO2 emissions estimate from Mexico City using ground- and space-
958 based remote sensing. submitted to Journal of Geophysical Research.
959 Che, K., Lauvaux, T., Taquet, N., Stremme, W., Xu, Y., Alberti, C., Lopez, M., García-Reynoso, A., Ciais, P.,
960 Liu,Y., Ramonet, M., Grutter, M. (2024). Urban XCO2 gradients from a dense network of solar absorption
961 spectrometers and OCO-3 over Mexico City. Journal of Geophysical Research: Atmospheres, 129(9),
962 e2023JD040063.,https://doi.org/10.1029/2023JD040063

Chen, J., Viatte, C., Hedelius, J. K., Jones, T., Franklin, J. E., Parker, H., Gottlieb, E. W., Wennberg, P. O., Dubey, M. K., and Wofsy, S. C.: Differential column measurements using compact solar-tracking spectrometers, Atmos. Chem. Phys., 16, 8479–8498, https://doi.org/10.5194/acp-16-8479-2016, 2016.

Chevallier, F., Deutscher, N. M., Conway, T. J., Ciais, P., Ciattaglia, L., Dohe, S., Fröhlich, M., Gomez-Pelaez, A. J., Griffith, D., Hase, F., Haszpra, L., Krummel, P., Kyrö, E., Labuschagne, C., Langenfelds, R., Machida, T., Maignan, F., Matsueda, H., Morino, I., Notholt, J., Ramonet, M., Sawa, Y., Schmidt, M., Sherlock, V., Steele, P., Strong, K., Sussmann, R., Wennberg, P., Wofsy, S., Worthy, D., Wunch, D., and Zimnoch, M.: Global $CO_2$ fluxes inferred from surface air-sample measurements and from TCCON retrievals of the $CO_2$ total column: TWO $CO_2$ FLUX INVERSIONS, Geophys. Res. Lett., 38, n/a-n/a, https://doi.org/10.1029/2011GL049899, 2011.

de Foy, B., Varela, J. R., Molina, L. T., and Molina, M. J.: Rapid ventilation of the Mexico City basin and regional fate of the urban plume, Atmos. Chem. Phys., 6, 2321–2335, https://doi.org/10.5194/acp-6-2321-2006, 2006.

Duren, R. M. and Miller, C. E.: Measuring the carbon emissions of megacities, Nature Clim Change, 2, 560–562, https://doi.org/10.1038/nclimate1629, 2012.

Frey, M., Sha, M. K., Hase, F., Kiel, M., Blumenstock, T., Harig, R., Surawicz, G., Deutscher, N. M., Shiomi, K., Franklin, J. E., Bösch, H., Chen, J., Grutter, M., Ohyama, H., Sun, Y., Butz, A., Mengistu Tsidu, G., Ene, D., Wunch, D., Cao, Z., Garcia, O., Ramonet, M., Vogel, F., and Orphal, J.: Building the COllaborative Carbon Column Observing Network (COCCON): long-term stability and ensemble performance of the EM27/SUN Fourier transform spectrometer, Atmos. Meas. Tech., 12, 1513–1530, https://doi.org/10.5194/amt-12-1513-2019, 2019.

Frey, M. M., Hase, F., Blumenstock, T., Dubravica, D., Groß, J., Göttsche, F., Handjaba, M., Amadhila, P., Mushi, R., Morino, I., Shiomi, K., Sha, M. K., De Mazière, M., and Pollard, D. F.: Long-term column-averaged greenhouse gas observations using a COCCON spectrometer at the high-surface-albedo site in Gobabeb, Namibia, Atmos. Meas. Tech., 14, 5887–5911, https://doi.org/10.5194/amt-14-5887-2021, 2021.

García-Franco, J. L., Stremme, W., Bezanilla, A., Ruiz-Angulo, A., and Grutter, M.: Variability of the Mixed-Layer Height Over Mexico City, Boundary-Layer Meteorol, 167, 493–507, https://doi.org/10.1007/s10546-018-0334-x, 2018.

García-Franco, J. L.: Air quality in Mexico City during the fuel shortage of January 2019. Atmospheric environment, 222, 117131, 2020.

Gisi, M.: Setup of precise camera based solar tracker systems and greenhouse gas measurements using a modified portable spectrometer, https://doi.org/10.5445/IR/1000031248, 2012.

Gisi, M., Hase, F., Dohe, S., and Blumenstock, T.: Camtracker: a new camera controlled high precision solar tracker system for FTIR-spectrometers, Atmos. Meas. Tech., 4, 47–54, https://doi.org/10.5194/amt-4-47-2011, 2011.

Gisi, M., Hase, F., Dohe, S., Blumenstock, T., Simon, A., and Keens, A.: XCO2 measurements with a tabletop FTS using solar absorption spectroscopy, Atmos. Meas. Tech., 5, 2969–2980, https://doi.org/10.5194/amt-5-2969-2012, 2012.

Goldberg, D. L., Lu, Z., Oda, T., Lamsal, L. N., Liu, F., Griffin, D., McLinden, C. A., Krotkov, N. A., Duncan, B. N., and Streets, D. G.: Exploiting OMI NO2 satellite observations to infer fossil-fuel CO2 emissions from U.S. megacities, Science of The Total Environment, 695, 133805, https://doi.org/10.1016/j.scitotenv.2019.133805, 2019.

González Del Castillo, E., Taquet, N., Bezanilla, A., Stremme, W., Ramonet, M., Laurent, O, Xu, Y., Delmotte, M., Grutter, M.: CO2 variability in the Mexico City region from in situ measurements at an urban and a background site, Atm., 35, 377–393, https://doi.org/10.20937/ATM.52956, 2022.

Grutter, M.: Multi-Gas analysis of ambient air using FTIR spectroscopy over Mexico City, Atmosfera, 16, 1–13, 2003.

Grutter, M., Rivera, O., Retama, A., Contreras, J., González, E., Porras, S., López, O., Arredondo, T., Díaz, A., Robles, M., Sánchez B., Azpra, E., Ladino, L. Technical Report #4 in "EVALUACIÓN DE DISPOSITIVOS BASADOS EN MICROSENSORES PARA EL MONITOREO CONTINUO DE LA CALIDAD DEL AIRE", ICAyCC-UNAM 2023.

Grutter, M., Flores, E., Basaldud, R., & Ruiz-Suárez, L. G. (2003). Open-path FTIR spectroscopic studies of the trace gases over Mexico City. *ATMOSPHERIC AND OCEANIC OPTICS C/C OF OPTIKA ATMOSFERY I OKEANA*, *16*(3), 232-236.

Gurney, K. R., Liang, J., O'Keeffe, D., Patarasuk, R., Hutchins, M., Huang, J., Rao, P., and Song, Y.: Comparison of Global Downscaled Versus Bottom-Up Fossil Fuel $CO_2$ Emissions at the Urban Scale in Four U.S. Urban Areas, JGR Atmospheres, 124, 2823–2840, https://doi.org/10.1029/2018JD028859, 2019.

Hakkarainen, J., Szeląg, M. E., Ialongo, I., Retscher, C., Oda, T., and Crisp, D.: Analyzing nitrogen oxides to carbon dioxide emission ratios from space: A case study of Matimba Power Station in South Africa, Atmospheric Environment: X, 10, 100110, https://doi.org/10.1016/j.aeaoa.2021.100110, 2021.

Hardy, C. C.: Smoke management guide for prescribed and wildland fire, National Wildlife Coordinating Group, 2001.

Hase, F., Hannigan, J. W., Coffey, M. T., Goldman, A., Höpfner, M., Jones, N. B., Rinsland, C. P., and Wood, S. W.: Intercomparison of retrieval codes used for the analysis of high-resolution, ground-based FTIR measurements, Journal of Quantitative Spectroscopy and Radiative Transfer, 87, 25–52, https://doi.org/10.1016/j.jqsrt.2003.12.008, 2004.

Hase, F., Frey, M., Blumenstock, T., Groß, J., Kiel, M., Kohlhepp, R., Mengistu Tsidu, G., Schäfer, K., Sha, M. K., and Orphal, J.: Application of portable FTIR spectrometers for detecting greenhouse gas emissions of the major city Berlin, Atmos. Meas. Tech., 8, 3059–3068, https://doi.org/10.5194/amt-8-3059-2015, 2015.

Hase, F., Frey, M., Kiel, M., Blumenstock, T., Harig, R., Keens, A., and Orphal, J.: Addition of a channel for XCO observations to a portable FTIR spectrometer for greenhouse gas measurements, Atmospheric Measurement Techniques, 9, 2303–2313, 2016.

Hedelius, J. K., Viatte, C., Wunch, D., Roehl, C. M., Toon, G. C., Chen, J., Jones, T., Wofsy, S. C., Franklin, J. E., Parker, H., Dubey, M. K., and Wennberg, P. O.: Assessment of errors and biases in retrievals of $XCO_2$, $XCH_4$, XCO, and $XN_2O$ from a 0.5 $cm^{-1}$ resolution solar-viewing spectrometer, Atmos. Meas. Tech., 9, 3527–3546, https://doi.org/10.5194/amt-9-3527-2016, 2016.

Hedelius, J. K., Liu, J., Oda, T., Maksyutov, S., Roehl, C. M., Iraci, L. T., Podolske, J. R., Hillyard, P. W., Liang, J., Gurney, K. R., Wunch, D., and Wennberg, P. O.: Southern California megacity $CO_2$, $CH_4$, and CO flux estimates using ground- and space-based remote sensing and a Lagrangian model, Atmos. Chem. Phys., 18, 16271–16291, https://doi.org/10.5194/acp-18-16271-2018, 2018.

Hernández-Paniagua, I. Y., Valdez, S. I., Almanza, V., Rivera-Cárdenas, C., Grutter, M., Stremme, W., García Reynoso, A., Ruiz-Suárez, L. G. (2021). Impact of the COVID-19 lockdown on air quality and resulting public health benefits in the Mexico City metropolitan area. Frontiers in public health, 9, 642630.

Herrera, B., Bezanilla, A., Blumenstock, T., Dammers, E., Hase, F., Clarisse, L., Magaldi, A., Rivera, C., Stremme, W., Strong, K., Viatte, C., Van Damme, M., and Grutter, M.: Measurement report: Evolution and distribution of $NH_3$ over Mexico City from ground-based and satellite infrared spectroscopic measurements, Atmos. Chem. Phys., 22, 14119–14132, https://doi.org/10.5194/acp-22-14119-2022, 2022.

Hersbach, H., Bell, B., Berrisford, P., Hirahara, S., Horányi, A., Muñoz-Sabater, J., Nicolas, J., Peubey, C., Radu, R., Schepers, D., Simmons, A., Soci, C., Abdalla, S., Abellan, X., Balsamo, G., Bechtold, P., Biavati, G., Bidlot, J., Bonavita, M., De Chiara, G., Dahlgren, P., Dee, D., Diamantakis, M., Dragani, R., Flemming, J., Forbes, R., Fuentes, M., Geer, A., Haimberger, L., Healy, S., Hogan, R. J., Hólm, E., Janisková, M., Keeley, S., Laloyaux, P., Lopez, P., Lupu, C., Radnoti, G., De Rosnay, P., Rozum, I., Vamborg, F., Villaume, S., and Thépaut, J.: The ERA5 global reanalysis, Quart J Royal Meteoro Soc, 146, 1999–2049, https://doi.org/10.1002/qj.3803, 2020.

Jones, C. D., Hickman, J. E., Rumbold, S. T., Walton, J., Lamboll, R. D., Skeie, R. B., Fiedler, S., Forster, P. M., Rogelj, J., Abe, M., Botzet, M., Calvin, K., Cassou, C., Cole, J. N. S., Davini, P., Deushi, M., Dix, M., Fyfe, J. C., Gillett, N. P., Ilyina, T., Kawamiya, M., Kelley, M., Kharin, S., Koshiro, T., Li, H., Mackallah, C., Müller, W. A., Nabat, P., Van Noije, T., Nolan, P., Ohgaito, R., Olivié, D., Oshima, N., Parodi, J., Reerink, T. J., Ren, L., Romanou, A., Séférian, R., Tang, Y., Timmreck, C., Tjiputra, J., Tourigny, E., Tsigaridis, K., Wang, H., Wu, M., Wyser, K., Yang, S., Yang, Y., and Ziehn, T.: The Climate Response to Emissions Reductions Due to COVID-19: Initial Results From CovidMIP, Geophysical Research Letters, 48, e2020GL091883, https://doi.org/10.1029/2020GL091883, 2021.

Kiel, M., Eldering, A., Roten, D. D., Lin, J. C., Feng, S., Lei, R., Lauvaux, T., Oda, T., Roehl, C. M., Blavier, J.-F., and Iraci, L. T.: Urban-focused satellite CO2 observations from the Orbiting Carbon Observatory-3: A first look at the Los Angeles megacity, Remote Sensing of Environment, 258, 112314, https://doi.org/10.1016/j.rse.2021.112314, 2021.

Kutralam-Muniasamy, G., Pérez-Guevara, F., Roy, P. D., Elizalde-Martínez, I., and Shruti, V. C.: Impacts of the COVID-19 lockdown on air quality and its association with human mortality trends in megapolis Mexico City, Air Qual Atmos Health, 14, 553–562, https://doi.org/10.1007/s11869-020-00960-1, 2021.

Le Quéré, C., Jackson, R. B., Jones, M. W., Smith, A. J. P., Abernethy, S., Andrew, R. M., De-Gol, A. J., Willis, D. R., Shan, Y., Canadell, J. G., Friedlingstein, P., Creutzig, F., and Peters, G. P.: Temporary reduction in daily global CO2 emissions during the COVID-19 forced confinement, Nat. Clim. Chang., 10, 647–653, https://doi.org/10.1038/s41558-020-0797-x, 2020.

Lei, R., Feng, S., Danjou, A., Broquet, G., Wu, D., Lin, J. C., O'Dell, C. W., and Lauvaux, T.: Fossil fuel CO2 emissions over metropolitan areas from space: A multi-model analysis of OCO-2 data over Lahore, Pakistan, Remote Sensing of Environment, 264, 112625, https://doi.org/10.1016/j.rse.2021.112625, 2021.

Lian, J., Lauvaux, T., Utard, H., Bréon, F.-M., Broquet, G., Ramonet, M., Laurent, O., Albarus, I., Chariot, M., Kotthaus, S., Haeffelin, M., Sanchez, O., Perrussel, O., Denier Van Der Gon, H. A., Dellaert, S. N. C., and Ciais, P.: Can we use atmospheric $CO_2$ measurements to verify emission trends reported by cities? Lessons from a six-

year atmospheric inversion over Paris, Gases/Atmospheric Modelling and Data Analysis/Troposphere/Physics (physical properties and processes), https://doi.org/10.5194/egusphere-2023-401, 2023.

Liu, Z., Ciais, P., Deng, Z., Lei, R., Davis, S. J., Feng, S., Zheng, B., Cui, D., Dou, X., Zhu, B., Guo, R., Ke, P., Sun, T., Lu, C., He, P., Wang, Y., Yue, X., Wang, Y., Lei, Y., Zhou, H., Cai, Z., Wu, Y., Guo, R., Han, T., Xue, J., Boucher, O., Boucher, E., Chevallier, F., Tanaka, K., Wei, Y., Zhong, H., Kang, C., Zhang, N., Chen, B., Xi, F., Liu, M., Bréon, F.-M., Lu, Y., Zhang, Q., Guan, D., Gong, P., Kammen, D. M., He, K., and Schellnhuber, H. J.: Near-real-time monitoring of global CO2 emissions reveals the effects of the COVID-19 pandemic, Nat Commun, 11, 5172, https://doi.org/10.1038/s41467-020-18922-7, 2020.

Lu, S., Wang, J., Wang, Y., and Yan, J.: Analysis on the variations of atmospheric $CO_2$ concentrations along the urban–rural gradients of Chinese cities based on the OCO-2 $XCO_2$ data, International Journal of Remote Sensing, 39, 4194–4213, https://doi.org/10.1080/01431161.2017.1415482, 2018.

MacDonald, C. G., Mastrogiacomo, J.-P., Laughner, J. L., Hedelius, J. K., Nassar, R., and Wunch, D.: Estimating enhancement ratios of nitrogen dioxide, carbon monoxide and carbon dioxide using satellite observations, Atmos. Chem. Phys., 23, 3493–3516, https://doi.org/10.5194/acp-23-3493-2023, 2023.

Makarova, M. V., Alberti, C., Ionov, D. V., Hase, F., Foka, S. C., Blumenstock, T., Warneke, T., Virolainen, Y. A., Kostsov, V. S., Frey, M., Poberovskii, A. V., Timofeyev, Y. M., Paramonova, N. N., Volkova, K. A., Zaitsev, N. A., Biryukov, E. Y., Osipov, S. I., Makarov, B. K., Polyakov, A. V., Ivakhov, V. M., Imhasin, H. Kh., and Mikhailov, E. F.: Emission Monitoring Mobile Experiment (EMME): an overview and first results of the St. Petersburg megacity campaign-2019, Gases/Remote Sensing/Instruments and Platforms, https://doi.org/10.5194/amt-2020-87, 2020.

Molina, L. T., Madronich, S., Gaffney, J. S., Apel, E., De Foy, B., Fast, J., Ferrare, R., Herndon, S., Jimenez, J. L., Lamb, B., Osornio-Vargas, A. R., Russell, P., Schauer, J. J., Stevens, P. S., Volkamer, R., and Zavala, M.: An overview of the MILAGRO 2006 Campaign: Mexico City emissions and their transport and transformation, Atmos. Chem. Phys., 10, 8697–8760, https://doi.org/10.5194/acp-10-8697-2010, 2010.

Molina, L. T. Introductory lecture: air quality in megacities. Faraday discussions, 226, 9-52, 2021.

Park, H., Jeong, S., Park, H., Labzovskii, L. D., and Bowman, K. W.: An assessment of emission characteristics of Northern Hemisphere cities using spaceborne observations of CO2, CO, and NO2, Remote Sensing of Environment, 254, 112246, https://doi.org/10.1016/j.rse.2020.112246, 2021.

Porras, S., González del Castillo, M.E., López, O., Arredondo, T., Rivera, O., Ramonet, M., Laurent, O., Grutter, M.: Diseño y despliegue de una red piloto para la medición de CO2 con un sistema de microsensores, UNAM internal report, 2023: http://www.epr.atmosfera.unam.mx/Microsensores-2022/documentos/4_Red_piloto_CO2.pdf (last accessed on May 20, 2024)

Plaza-Medina, E. F., Stremme, W., Bezanilla, A., Grutter, M., Schneider, M., Hase, F., and Blumenstock, T.: Ground-based remote sensing of O3 by high- and medium-resolution FTIR spectrometers over the Mexico City basin, Atmos. Meas. Tech., 10, 2703–2725, https://doi.org/10.5194/amt-10-2703-2017, 2017.

Pougatchev, N. S., Jones, N. B., Connor, B. J., Rinsland, C. P., Becker, E., Coffey, M. T., Connors, V. S., Demoulin, P., Dzhola, A. V., Fast, H., Grechko, E. I., Hannigan, J. W., Koike, M., Kondo, Y., Mahieu, E., Mankin, W. G., Mittermeier, R. L., Notholt, J., Reichle, H. G., Sen, B., Steele, L. P., Toon, G. C., Yurganov, L. N., Zander, R., and Zhao, Y.: Ground-based infrared solar spectroscopic measurements of carbon monoxide during 1994 Measurement of Air Pollution From Space flights, J. Geophys. Res., 103, 19317–19325, https://doi.org/10.1029/97JD02889, 1998.

Rinsland, C. P., Jones, N. B., Connor, B. J., Logan, J. A., Pougatchev, N. S., Goldman, A., Murcray, F. J., Stephen, T. M., Pine, A. S., Zander, R., Mahieu, E., and Demoulin, P.: Northern and southern hemisphere ground-based infrared spectroscopic measurements of tropospheric carbon monoxide and ethane, J. Geophys. Res., 103, 28197–28217, https://doi.org/10.1029/98JD02515, 1998.

Rißmann, M., Chen, J., Osterman, G., Zhao, X., Dietrich, F., Makowski, M., Hase, F., and Kiel, M.: Comparison of OCO-2 target observations to MUCCnet – is it possible to capture urban XCO2 gradients from space?, Atmos. Meas. Tech., 15, 6605–6623, https://doi.org/10.5194/amt-15-6605-2022, 2022.

Rivera Cárdenas, C., Guarín, C., Stremme, W., Friedrich, M. M., Bezanilla, A., Rivera Ramos, D., Mendoza-Rodríguez, C. A., Grutter, M., Blumenstock, T., and Hase, F.: Formaldehyde total column densities over Mexico City: comparison between multi-axis differential optical absorption spectroscopy and solar-absorption Fourier transform infrared measurements, Atmos. Meas. Tech., 14, 595–613, https://doi.org/10.5194/amt-14-595-2021, 2021.

Rodgers, C. D.: Inverse Methods for Atmospheric Sounding: Theory and Practice, WORLD SCIENTIFIC, https://doi.org/10.1142/3171, 2000.

Sha, M. K., De Mazière, M., Notholt, J., Blumenstock, T., Chen, H., Dehn, A., Griffith, D. W. T., Hase, F., Heikkinen, P., Hermans, C., Hoffmann, A., Huebner, M., Jones, N., Kivi, R., Langerock, B., Petri, C., Scolas, F., Tu, Q., and Weidmann, D.: Intercomparison of low- and high-resolution infrared spectrometers for ground-based solar remote sensing measurements of total column concentrations of CO2, CH4 and CO, Atmos. Meas. Tech., 13, 4791–4839, https://doi.org/10.5194/amt-13-4791-2020, 2020.

1141    Silva, S. J., Arellano, A. F., and Worden, H. M.: Toward anthropogenic combustion emission constraints from
1142    space-based analysis of urban CO $_2$ /CO sensitivity, Geophysical Research Letters, 40, 4971–4976,
1143    https://doi.org/10.1002/grl.50954, 2013.
1144    Storey, M. A. and Price, O. F.: Prediction of air quality in Sydney, Australia as a function of forest fire load
1145    and weather using Bayesian statistics, PLoS ONE, 17, e0272774, https://doi.org/10.1371/journal.pone.0272774,
1146    2022.
1147    Stremme, W., Ortega, I., and Grutter, M.: Using ground-based solar and lunar infrared spectroscopy to study
1148    the diurnal trend of carbon monoxide in the Mexico City boundary layer, Atmos. Chem. Phys., 9, 8061–8078,
1149    https://doi.org/10.5194/acp-9-8061-2009, 2009.
1150    Stremme, W., Grutter, M., Rivera, C., Bezanilla, A., Garcia, A. R., Ortega, I., George, M., Clerbaux, C.,
1151    Coheur, P.-F., Hurtmans, D., Hannigan, J. W., and Coffey, M. T.: Top-down estimation of carbon monoxide
1152    emissions from the Mexico Megacity based on FTIR measurements from ground and space, Atmos. Chem. Phys.,
1153    13, 1357–1376, https://doi.org/10.5194/acp-13-1357-2013, 2013.
1154    Su, T., Li, Z., and Kahn, R.: Relationships between the planetary boundary layer height and surface pollutants
1155    derived from lidar observations over China: regional pattern and influencing factors, Atmos. Chem. Phys., 18,
1156    15921–15935, https://doi.org/10.5194/acp-18-15921-2018, 2018.
1157    Sussmann, R. and Rettinger, M.: Can We Measure a COVID-19-Related Slowdown in Atmospheric CO2
1158    Growth? Sensitivity of Total Carbon Column Observations, Remote Sensing, 12, 2387,
1159    https://doi.org/10.3390/rs12152387, 2020.
1160    Toon, G., Blavier, J.-F., Washenfelder, R., Wunch, D., Keppel-Aleks, G., Wennberg, P., Connor, B., Sherlock,
1161    V., Griffith, D., Deutscher, N., and Notholt, J.: Total Column Carbon Observing Network (TCCON), in: Advances
1162    in Imaging, Advances in Imaging, Vancouver, journalAbbreviation: HISensE, JMA3, 2009.
1163    Viatte, C., Lauvaux, T., Hedelius, J. K., Parker, H., Chen, J., Jones, T., Franklin, J. E., Deng, A. J., Gaudet, B.,
1164    Verhulst, K., Duren, R., Wunch, D., Roehl, C., Dubey, M. K., Wofsy, S., and Wennberg, P. O.: Methane emissions
1165    from dairies in the Los Angeles Basin, Atmos. Chem. Phys., 17, 7509–7528, https://doi.org/10.5194/acp-17-7509-
1166    2017, 2017.
1167    Vogel, F. R., Frey, M., Staufer, J., Hase, F., Broquet, G., Xueref-Remy, I., Chevallier, F., Ciais, P., Sha, M. K.,
1168    Chelin, P., Jeseck, P., Janssen, C., Té, Y., Groß, J., Blumenstock, T., Tu, Q., and Orphal, J.:
1169    XCO<sub>2</sub> in an emission hot-spot region: the COCCON Paris campaign 2015, Atmos. Chem.
1170    Phys., 19, 3271–3285, https://doi.org/10.5194/acp-19-3271-2019, 2019.
1171    Wang, H., Jiang, F., Wang, J., Ju, W., and Chen, J. M.: Terrestrial ecosystem carbon flux estimated using
1172    GOSAT and OCO-2 XCO<sub>2</sub> retrievals, Atmos. Chem. Phys., 19, 12067–12082,
1173    https://doi.org/10.5194/acp-19-12067-2019, 2019.
1174    Wang, Y., Broquet, G., Bréon, F.-M., Lespinas, F., Buchwitz, M., Reuter, M., Meijer, Y., Loescher, A.,
1175    Janssens-Maenhout, G., Zheng, B., and Ciais, P.: PMIF v1.0: assessing the potential of satellite observations to
1176    constrain CO2; emissions from large cities and point sources over the globe using synthetic data, Geosci. Model
1177    Dev., 13, 5813–5831, https://doi.org/10.5194/gmd-13-5813-2020, 2020.
1178    Wu, D., Lin, J. C., Fasoli, B., Oda, T., Ye, X., Lauvaux, T., Yang, E. G., and Kort, E. A.: A Lagrangian
1179    approach towards extracting signals of urban CO2 emissions from satellite observations of atmospheric column
1180    CO2 (XCO2): X-Stochastic Time-Inverted Lagrangian Transport model ("X-STILT v1"), Geosci. Model Dev.,
1181    11, 4843–4871, https://doi.org/10.5194/gmd-11-4843-2018, 2018.
1182    Wunch, D., Wennberg, P. O., Toon, G. C., Keppel-Aleks, G., and Yavin, Y. G.: Emissions of greenhouse gases
1183    from a North American megacity, Geophysical Research Letters, 36, 2009GL039825,
1184    https://doi.org/10.1029/2009GL039825, 2009.
1185    Xu, Y., Lauvaux T., Grutter, M., Taquet, N., García-Reynoso, J.A., Laurent, O., Lopez, M., Lian, J., Lin, X.,
1186    Stremme, W., Ramonet, M., Atmospheric CO2 dynamics over a mountain urban basin: a case study of the Mexico
1187    City metropolitan area, submitted.
1188    Ye, X., Lauvaux, T., Kort, E. A., Oda, T., Feng, S., Lin, J. C., Yang, E., and Wu, D.: Constraining fossil fuel
1189    CO<sub>2</sub> emissions from urban area using OCO-2 observations of total column
1190    CO<sub>2</sub>, Gases/Atmospheric Modelling/Troposphere/Physics (physical properties and
1191    processes), https://doi.org/10.5194/acp-2017-1022, 2017.
1192    You, Y., Byrne, B., Colebatch, O., Mittermeier, R. L., Vogel, F., and Strong, K.: Quantifying the Impact of the
1193    COVID-19 Pandemic Restrictions on CO, CO2, and CH4 in Downtown Toronto Using Open-Path Fourier
1194    Transform Spectroscopy, Atmosphere, 12, 848, https://doi.org/10.3390/atmos12070848, 2021.
1195    Zhang, Q., Boersma, K. F., Zhao, B., Eskes, H., Chen, C., Zheng, H., and Zhang, X.: Quantifying daily NO $_x$
1196    and CO $_2$ emissions from Wuhan using satellite observations from TROPOMI and OCO-2, Atmos. Chem. Phys.,
1197    23, 551–563, https://doi.org/10.5194/acp-23-551-2023, 2023.
1198    Zhao, X., Marshall, J., Hachinger, S., Gerbig, C., Frey, M., Hase, F., and Chen, J.: Analysis of total column
1199    CO2 and CH4 measurements in Berlin with WRF-GHG, Atmos. Chem. Phys., 19, 11279–11302,
1200    https://doi.org/10.5194/acp-19-11279-2019, 2019.

1201    Zhou, M., Ni, Q., Cai, Z., Langerock, B., Nan, W., Yang, Y., Che, K., Yang, D., Wang, T., Liu, Y., and Wang,
1202    P.: CO2 in Beijing and Xianghe Observed by Ground-Based FTIR Column Measurements and Validation to OCO-
1203    2/3 Satellite Observations, Remote Sensing, 14, 3769, https://doi.org/10.3390/rs14153769, 2022.
1204